NTNU – Trondheim
Norwegian University of
Science and Technology

Investigation of Carbon Block/Cast Iron/Collector Bar Interfaces in Aluminum Electrolysis

Ahmet Oguz Tezel

Light Metals Production
Submission date: June 2012
Supervisor: Odd-Arne Lorentsen, IMTE
Co-supervisor: Eirik Hagen, Hydro Aluminium

Norwegian University of Science and Technology
Department of Materials Science and Engineering

Investigation of Carbon Cathode / Cast iron / Collector Bar Interfaces in Aluminum Electrolysis

by

Ahmet Oguz Tezel

Submitted to the Department of Materials Science and Engineering
in Partial Fulfillment of the Requirements for the Degree of
Master of Science in Materials Science and Engineering

at the

Norwegian University of Science and Technology

June, 2012

Thesis Supervisor: Prof. Odd-Arne Lorentsen
Title: R&D Program Manager at HYDRO Aluminium A.S. & Adjunct Professor at the Norwegian University of Science and Technology

Co-Supervisor: Dr. Eirik Hagen
Title: Principle Engineer at HYDRO Aluminium A.S.

ACKNOWLEDGEMENT

This work was carried out at the Department of Materials Science and Engineering at Norwegian University of Science and Technology in collaboration with HYDRO Aluminium. This thesis was part of the research program entitled 'HAL UP' at HYDRO Aluminium.

I owe the largest depth of gratitude to my supervisor, Prof. Odd-Arne Lorentsen for his constant support, inspiration and encouragement in the past two years. I am immensely pleased to have had the privilege to have known and worked with him. He, without whom it would hardly possible for me to finish this task and graduate, has been a wonderful supervisor and a friend to me. From the very depth of my heart I am thankful to him for the opportunities he provided me; because I believe we are only as great as the opportunities that are given to us.

Thanks are also due to my co-supervisor Dr. Eirik Hagen of Hydro Aluminum for providing the samples that made this thesis available and for his valuable comments on my findings.

I would like to thank Dr. Julian Tolchard for passionately teaching me how to best utilize the SEM and the EDX. It must have been very tough to answer all the questions and confusions I had about the electronic structure of the materials.

Thanks should be extended to Bjarte Øye and Ove Darell for their help in handling the samples and especially for letting me use the cutting saw.

My heartfelt thanks are also extended to the PhD candidates at the Department of Materials Science and Engineering who have always been available to answer and guide me whenever I needed a guidance.

Last, but not least, I thank to Belde Mutaf for making the things through.

Trondheim, June 2012

Ahmet Oguz Tezel

TABLE OF CONTENTS

List of Figures

List of Tables

SUMMARY

The chemical events occurring at the carbon/cast iron/collector bar interface that might have an impact on the cathodic voltage drop in aluminum electrolysis is elucidated in this thesis. The primary aluminum production is an energy intensive process which constantly requires to bring as high an energy efficient development as possible in order to be competitive. The cathodic voltage drop represents ~10% of the overall energy consumption of the process. Among the measures to reduce the voltage drop, the collector bar and its surroundings need to be investigated as the literature on this part of the assembly is very narrow.

In this thesis, the microstructural and compositional evolution of the cast irons and the collector bars taken from the cells that were shut down after 7 days and 2190 days (6 years) in operation is presented using the analytical tools such as SEM, EDX and optic microscope. The effect of this evolution on the voltage drop is then evaluated by referring to the electrical conductivities of the observed phases and microstructures.

The penetration of the bath components, especially aluminum (as high as 14wt.% in the cast iron and 0.44wt.% in the steel) and sodium (1.38wt.% in the cast iron and 0.02wt.% in the steel), into the cast iron and the steel was found partly linked to the morphology of the graphite in the cast iron. The kinetics of the development of the morphology of the graphite was suspected to be determined by the presence of the magnetic field or the magnetic field gradient. It was also shown that the magnetic field might cause a shift in the equilibrium Fe-C diagram. In this respect, stabilization of the ferrite over the austenite is noteworthy as its resistivity is ~one third the resistivity of the austenite (0.1μΩm *vs* 0.34 μΩm at 300K and 313K respectively).

High phosphorous cast iron was found to form liquid eutectics that preferentially settle at the grain boundaries. This phase is regarded to have a negative effect both on the contact pressure and on the electrical conductivity. Therefore it is suggested to employ lower P containing cast iron grades as the rodding material.

1. INTRODUCTION

1.1. Motivation

Aluminum, of the metallic elements, is the most abundant one (8.1 mass %) in the earth's crust (1). The unique properties it possesses such as, strength, lightness, corrosion resistance, makes it the most versatile and vital material for our modern society. It is almost one third as dense as iron, while some of its alloys are as strong as mild steel. It finds numerous application areas, including electrical Industry (as the replacement of copper), automotive and aircraft industries, construction industry etc. It would be inappropriate to envision a future without aluminum.

Due to its high affinity towards oxygen, it is not found in nature in its elemental state, but as oxides or silicates (2). Therefore, its production involves a multi-step process route; alumina, Al_2O_3, extraction from Bauxite that contains gibbsite, boehmite and diaspore, through *Bayer Process* and electrolysis of alumina by *Hall-Hèroult Process.*

Hall-Hèroult Process is an energy intensive process which requires about 13.2 *kWh/kg* Al for given cell design and operational parameters (3). In order to be competitive in an era facing energy shortage, aluminum industry needs to achieve a dramatic reduction in the cell voltage. However most of the proposed reduction strategies (such as inert electrodes) involve significant changes in the cell design and bath chemistry, implementation of which demand large investment pledges by the industry.

Cathode voltage drop, CVD, constitutes 10-15% (0.3-0.5*V*) (4) of the overall power consumption of a typical reduction cell, just coming after the reversible cell potential (1.22*V*) and electrolyte voltage (1.34*V*) (3). Moreover, the cathode life is in an increasing trend (4) and this fact adds to CVD in the cells with aging cathodes. Among the other factors, the contact resistance at collector bar/cast iron/carbon interface is a major contributor to CVD (4).

Furthermore, due to the bath penetration into the cast iron and steel, electrical properties of these parts alter with time. The change of the chemistry of the cast iron and the bar due to the alloying with the components of the penetrated bath and its implications need to be elucidated. The very first step to take is to establish a complete picture of the chemistry spanning the cast iron and the steel bar. Publications referred to this problem is very narrow, therefore the study of these interfaces to develop a thorough understanding of the reactions that lead to increased electrical resistance is necessary.

1.2. Hall-Hèroult Process

The primary aluminum is produced in alumina reduction cells (Figure 1) by the *Hall-Hèroult Process.* It takes its name from its inventors, Paul Hèroult of France and Charles Martin Hall of U.S.A , who independently of each other discovered and patented the process in 1886. Both claimed to produce aluminum by passing current through a molten bath (Al_2O_3 + Na_3AlF_6) at a temperature about 970^0C (Further details of bath composition is provided in 1.2.1 ELECTROLYTE). At the cathode, liquid aluminum metal is produced, and at the anode carbon dioxide gas is produced according to the reaction 1.1

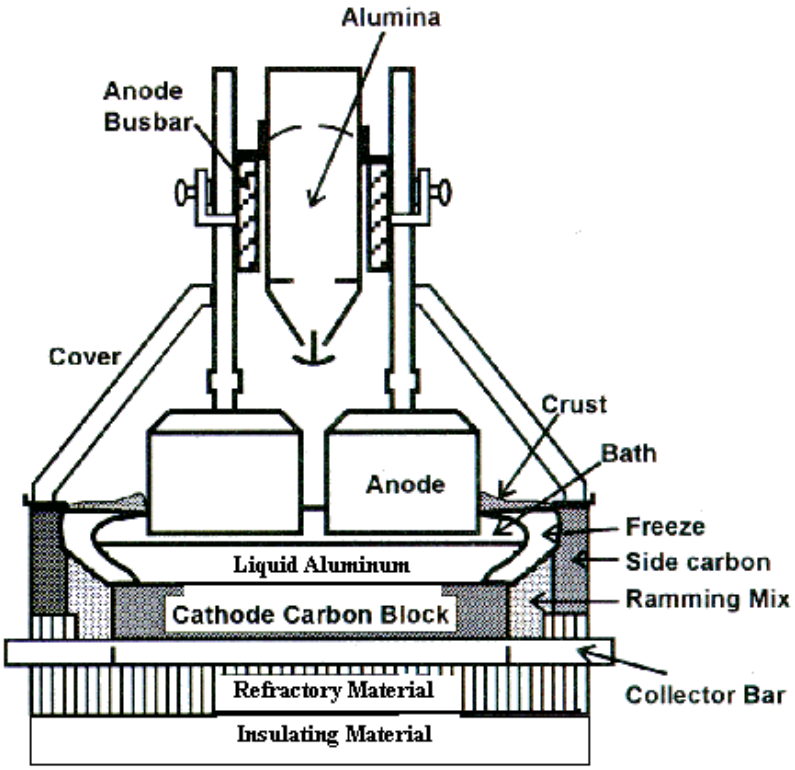

Figure 1.1: Schematic of an alumina reduction cell (Prebaked). Adopted from (5).

$$Al_2O_{3(diss.)} + {}^3/_4\, C_3 \Rightarrow Al_{(l)} + {}^3/_4\, CO_{2(g)} \qquad [1.1]$$

1.2.1. Electrolyte

1.2.1.1. Electrolysis in Aqueous Media

Water is the most plentiful solvent (6) and thereby is utilized in many hydrometallurgical processes (Zinc electrowinning, Ni electroplating). However the major drawback encountered with the use of water in the electrolytic processes is that many industrially relevant metals, particularly those from the early main groups of the periodic table are positioned higher up (more negative) in the EMF series than the hydrogen, thus giving rise to liberation of hydrogen gas (Equation 1.2) as the by-product at the cathode (7). This is an undesired reaction because it consumes current and reduces the current efficiency of the process with respect to the desired metal.

$$2H^+_{(diss.)} + 2e^- \Rightarrow H_{2(g)} \qquad [1.2]$$

Alumina is the raw material from which aluminum is electrolytically extracted and has, unfortunately, a melting point as high as 2050^0C and higher decomposition voltage (1.22 V) than the water. Thereby carrying out an electrolytic process in molten alumina as conducting media would pose a difficulty in developing suitable cell materials that could withstand this temperature. Furthermore, heat loss through thermal radiation would be economically detrimental for the industry (7). Therefore a solvent with relatively low melting temperature is inevitable for alumina electrolysis.

1.2.1.2. Electrolysis in Nonaqueous Media: Molten Salts

Molten salts are basically high temperature liquids and are mainly used as solvents or electrolytes in high temperature electrochemistry. To clarify, we should mention that there are some classes of high temperature liquids that are not regarded as molten salts, such as oxides and sulfides; what remain left are halide melts and ionic melts with complex anions (sulfates, nitrates, carbonates) with the latter one having anions that are easy to decompose anodically (8). Hence what we have are the halide melts to utilize for electrowinning processes.

The foregoing attractiveness of molten halides for electrowinning processes is the specific conductivity they display, which is, about 10^8 times higher than that of molten ice (6). Table 1.1 compares the specific conductivity of some molten halides with molten ice.

Much of the difficulties in handling the molten halides stems from the fact that they are extremely corrosive and require high operating temperatures. This in turn leads to the establishment of stringent materials selection criteria that is met only by very few materials. Melting temperatures of some of the industrially relevant inorganic salts are given in Table 1.2.

Table 1.1 Conductivities of Molten Salts and Water. Adapted from (6,9,10)

Substance	**Temperature (K)**	**Specific conductivity ($\Omega^{-1}m^{-1}$)**
H_2O	291	$4x10^{-8}$
$NaF\text{-}AlF_3$*	1023	1.27
$KF\text{-}AlF_3$†	1027	1.11
LiCl melt	983	6.221
NaCl melt	1181	3.903
KCl melt	1145	2.407

* C.R= 1.22, † C.R=1.3 (C.R=Cryolite ratio)

Table 1.2 Melting Temperatures of various inorganic salts (6,9,11)

Substance	Melting point (K)
$HgBr_2$	511
$ZnCl_2$	548
$HgCl_2$	550
$PbBr_2$	646
AgBr	707
LiCl	883
$3KF.AlF_3$	1258
$3NaF.AlF_3$	1284

1.2.1.3. Electrolyte used in Hall Héroult Process

The chemistry of the electrolyte is vital for the energy related studies since, to a considerable extent, almost one third of the cell voltage consists of the electrolyte voltage. Furthermore, the applicability of the inert electrode technology is deeply linked to the chemical composition and the liquidus temperature of the electrolyte used, because the rate of the corrosion is a function of these factors.

The electrolyte should perform the following functions (9);

- To carry the current from anode to the cathode,
- To be a solvent for alumina to enable its electrolytic decomposition, forming aluminum and carbon dioxide,
- To provide physical separation between the cathodically produced aluminum metal and the anodically evolved carbon dioxide gas,
- To behave as a heat-generating resistor that enables the cell to be self-heating.

Cryolite, Na_3AlF_6, is the main electrolyte constituent for alumina, Al_2O_3, electrolysis. It provides unique capacity to dissolve alumina. Table 1.3 demonstrates a comparison of alumina solubility in various halide melts as calculated by Skybakmoen *et al.*(12). Its physicochemical properties are modified by fluoride additives such as, magnesium fluoride,

MgF_2, calcium fluoride, CaF_2 and lithium fluoride, LiF. A typical bath composition is given in Table 1.4.

Table 1.3: Alumina solubility with varying electrolyte composition (12)

Composition* (wt%)	**Alumina solubility (wt%)**
AlF_3-CaF_2-LiF (0.0-0.0-0.0)	10.3
AlF_3-CaF_2-LiF (10.5-5.0-0.0)	8.0
AlF3-CaF_2-LiF (10.0-5.0-5.0)	5.5

* Rest being the cryolite, Na_3AlF_6

Table 1.4: Typical bath composition(1)

Compound	**Composition (wt%)**
Na_3AlF_6	80-85
AlF_3	10-12
CaF_2	4-6
Al_2O_3	2-3

It is worth noting that industry has been gradually decreasing the bath ratio (increasing AlF_3 content) aiming lower operating temperatures[1].

There have been many attempts (13) to replace the cryolite base electrolyte with those offering new opportunities for new technologies. The main thrust of these attempts was to improve the significantly low energy utilization of the process (less than 50% (13)); as the aluminum melts at 660^0C, operating the cells at temperature ranges greater than 700-800^0C means waste of energy in the form of heat loss. There are two proposal to mitigate the heat loss; designing a well-isolated cell and developing a low temperature electrolyte. A well-

[1] The temperature should be maintained well beyond the melting point of aluminum to prevent solidification while transferring the metal to the cast-house.

isolated cell is an interim solution, because it will in turn alter the heat balance of the cell and inhibit the side-ledge growth. Next is the development of a low temperature electrolyte, which is a quite complex and compelling task since it involves the consideration of physicochemical properties of the bath such as, ionic conductivity, density, stability towards cell materials, volatility, alumina solubility.

Of the candidate electrolyte systems with low melting temperatures, ionic liquids are to offer up to 85% save in electrical energy and reduce gaseous pollutants (e.g., CO, CF_4) as well as solid wastes(e.g., aluminum dross) (14). Various chloroaluminates such as $AlCl_3$-EMIC, $AlCl_3$-BPC and $AlCl_3$-NaCl-KCl are frequently studied in this purpose.

Another low melting electrolyte system is KF-AlF_3 system that enables electrolytic production of aluminum at temperature range as low as 700^0C. This system is of particular interest as it is considered indispensable for development of inert anode technology. It has been the main focus of many research team (10,15, 16,17) aiming to reveal its physicochemical properties and estimate its compatibility with inert anode materials under investigation. However, despite many advantageous like wide liquid window and low melting temperature it offers, the major shortcoming encountered with it is the dilution of K concentration by the Na coming into the cell with alumina (9). As the K is cost prohibitive, dilution of its concentration is a serious obstacle that must be overcome. It is also notable that K swelling of the cathode carbon is an issue to put into consideration.

1.2.2. Electrodes

Although the main source of the gaseous pollutants emitted from the Hall-Hèroult cells is the carbon, both anode and cathode is still made of carbonaceous materials. The following sections are meant to give a brief overview of the electrodes used in today's industry.

1.2.2.1. The Anodes

There are two different anode designs that find place in the cells; prebaked anodes and søderberg anodes, with the former being used predominantly. Among the reasons for the subordination of søderberg anodes in comparison to prebaked anodes are;

- size (amperage) limitations,
- higher carbon consumption,
- higher voltage drop,

- lower current efficiency,
- higher Aluminum metal contamination.

Prebaked anodes are made of a mixture of petroleum coke and coal tar pitch binder, molded into blocks and baked at about 1200^0C (For a thorough understanding of baking parameters and the resulting anode quality, consult (18)). They contain between 13-16wt% pitch (rest being petroleum coke), while the pitch content constitutes 25-28wt% in søderberg anodes (11). Prebaked anodes must be replaced with the new ones at regular intervals, usually after 30 days in service, when they are consumed down to one third of their original weight. Unlike the prebaked anodes, the Søderberg anodes are continuous self baking anodes. The green paste is briquetted and filled into rectangular steel anode casing of the cell and baked in the cell during the operation. It takes the briquettes approximately one month from the top to the bottom where it starts reacting with the bath. This self baking procedure is an advantageous in that anode baking facility is not required. Furthermore, heat loss arisen during the anode changing operation is eliminated, which results in higher energy utilization of the process.

Anode (petroleum coke) is also the primary source of the impurities that report to the bath and aluminum. Typical impurity concentration in petroleum coke is listed in Table1.5 (11).

Table 1.5 Typical impurity concentrations in petroleum coke(11)

Impurity	**Concentration (ppm)**	**Impurity**	**Concentration (ppm)**
Si	50-250	B	1
Fe	50-400	Na	30-120
Ti	2-50	Mg	100
Zn	2-20	C	20-100
V	30-350	Mn	4
Cr	1-2	Ga	14
Ni	50-220	Pb	3
Cu	1-3	Al	50-250
S	5000-35000	Ash	1000-2000

1.2.2.2. The Cathode

As it pertains to the scope of this thesis, the main focus is given to the cathode and the collector bar embedded in it, while the other aspects of aluminum electrolysis are briefly discussed. The discussion of the cathode in aluminum electrolysis poses many concept related challenges, especially when one makes an attempt to articulate what is the cathode. As depicted in Figure 1.1, the true cathode, which is in direct contact with the bath, is the liquid aluminum. Therefore, the passage of electric current is from the anodes immersed in the bath to the liquid metal and carbon cathodes successively. The development of magnetic forces, the product of current and magnetic field, due to the vertical action of the electrolysis current, gives rise to instability at metal/electrolyte interface. This unstable interface, in turn, will provoke increased mass transport with the resultant higher metal dissolution and lowering of current efficiency consequently (For a further discussion on magnetohydrodynamics of the cells, consult (19,20)).

Note that, from this point on, we adopt a terminology where cathode means the carbon block lying below the liquid aluminum. Thus the carbon block is part of the cell that completes the circuit through the collector bars. Given the above discussion, the cathode material that interacts with the liquid metal pad undoubtedly plays a determinative role in many aspects.

Today there are different starting materials for manufacturing of the bottom blocks, each possessing different qualities, namely, anthracite based blocks, graphitic blocks and graphitized blocks. The heat treatment processes they are subjected to differs as well, which lead to end products having substantially different properties (Figure 1.2). If one lists these materials in order of the performance of the end products, it follows; Anthracite based blocks, graphitic blocks and graphitized blocks, where graphitized being the most superior in many aspect. Anthracite based blocks contains various amounts of graphite, typically 30-50% (21). Graphite is added to amorphous or anthracitic bodies to improve the electrical conductivity. Graphite used in the manufacture of the graphitic blocks originates from scrap and/or is graphitized coke (21). The graphitized blocks use the calcined petroleum coke as starting material. The superiority of graphitized blocks over the others stems from the fact that it includes the impregnation of baked embodiment with pitch to reduce the porosity and an ensuing graphitization process that enables the graphitization of the pitch.

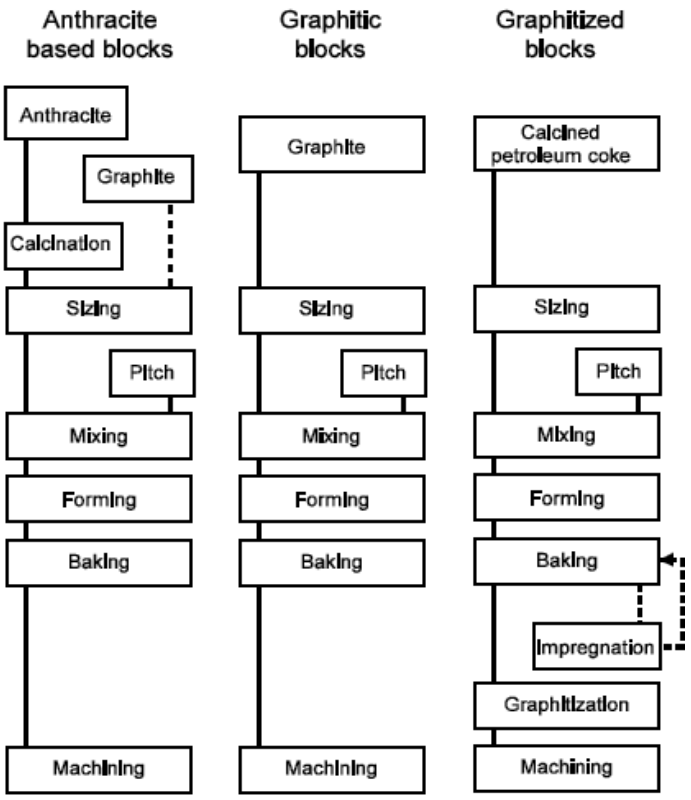

Figure 1.2 Flowsheets for cathode manufacturing (21)

The operational service life of an electrolysis cell may range 2000-3500 days (21) and is determined by operational and design parameters. To elaborate on and reveal the mechanisms governing the deterioration of the cathode lining, we should compartmentalize the carbon science into different branches because they have disparate concerns. The most important ones to the cathode are graphite-aluminum and graphite-alkali interactions as these interactions represent the main cathode deterioration process. The following concepts as tabulated by Liao (22), elucidate the cathode failure mechanisms;

- Swelling and crack propagation due to sodium absorption within carbon
- Cracking or upheaval of the cathode blocks resulting from the crystallization of salts during melt percolation
- Stratification of rammed parts, pothole formation and aluminum uptake in the cracks/potholes
- formation and dissolution of Al_4C_3 and physical abrasion of the carbon surface caused by sludge movement
- Breaking of the cathode lining due to thermal elongation and differential carbonization of the steel collector bar.

1.2.2.2.1. Chemical Reactions at the Cathode Carbon Surface and Bath Penetration into the Carbon Cathode

The reactions occurring at the carbon surface that lead to cathode deterioration are Al_4C_3 and Na formation, the former being limited within the surface, while the latter relates to the penetration into the cathode and causes further failure. The reaction between aluminum and carbon to yield Al_4C_3 is given by;

$$4Al_{(l)} + 3C_{(s)} = Al_4C_{3(s)} \quad [1.3]$$

At all temperatures of concern in aluminum production, reaction 1.3 is thermodynamically favored (23). However the amount of the carbide dissolved in the bath and aluminum is not as much as predicted by the equilibrium. The underlying reason for this is the suppression of the carbide formation reaction by a carbide layer of certain thickness formed over the carbon surface which mitigates the occurrence of contact between carbon and aluminum (24). An alternative explanation to the reduced rate of reaction was attributed by Dorward (25) to the presence of oxide layer between aluminum and carbon that controls the diffusion rate. This explanation was later argued by Sørlie and Øye (24) that under the reducing environment at the cathode surface the oxide formation would be unlikely. Alternatively, Gulbrandsen et.*al.*(26) suggested that the carbide may form due to the following electrochemical reaction;

$$C_{(s)} + 3AlF_{3(l)} + 4Na^+ + 4e^- = Na_3Al_3CF_{8(l)} + NaF_{(l)} \quad [1.4]$$

Na formation may arise as a result of either chemical (Equation 1.5) or electrochemical reaction (Equation 1.6) taking place on the liquid aluminum surface. Whether it is chemical or electrochemical was said to be a difficult task (27) to determine. Reaction 1.6 might also precede the reversal of the Reaction 1.5 (28).

$$Al_{(l)} + 3NaF_{(in\ cryolite\ )} = 3Na_{(in\ Al)} + AlF_{3(in\ cryolite\ )} \quad [1.5]$$

$$Na^+ + e^- = Na_{(in\ Al)} \quad [1.6]$$

Na penetration into the carbon block increases with bath ratio and current density (23). It reaches down to the collector bar and destroys the properties of the cast iron (see Discussions). On the other hand, melt penetration occurs as a result of sodium penetration; because sodium

increases the wettability of the carbon by the electrolyte. The melt is soaked in the carbon only within a few hours after the cell starts operation. Since there is a negative temperature gradient in the carbon block (temperature decreasing with depth), the soaked melt freezes at the isotherms where the temperature is below its liquidus temperature. This might result in heaving[2] of the carbon block (23). There are two main reactions[3] that take place within the carbon block (23);

$$2Na_{(3)}AlF_6 + 3Na_{(2)}O = Al_{(2)}O_3 + 12NaF \quad [1.7]$$

$$4Na_{(3)}AlF_6 + 12Na + 3C = Al_4C_3 + 24NaF \quad [1.8]$$

1.3. Reactions at the Carbon/Cast Iron/Collector Bar Interface and Literature Review

Although there is a wealth of literature written on the physical and chemical phenomena occurring at the surface of and within the carbon cathode, very rare have been dedicated to the carbon/cast iron/collector bar interface. As Prof. Jomar Thonstad suggested while in a conversation, it is hard to gather an expertise group consisting of both metallurgists and electrochemists. Because the cast iron and steel microstructures are difficult to interpret to an eye from outside the field of metallurgy, not many attempts have been made to study these interfaces.

Among the studies on the matter, Stagg (29) provided the first insight into the topic. He reported that aluminum forms upon the reaction 1.7 and diffuses into the bar surface forming 1% aluminum ferrite columnar grains and mechanically separate layer of aluminum rich phase on the outer surface of the bar. The grain boundary phase of the columnar grains was said to be $FeAl_3$, however this prediction was not based on the chemical analysis.

$$Na_3AlF_{6(l)} + 3Na_{(in\ C)} = 6NaF + Al_{(l)} \qquad \Delta G^0 = -41.7\ kJ\ at\ 950^0C \quad [1.9]$$

[2] Heaving is the term used to describe the physical deterioration of the carbon lining.
[3] Na_2O in the Reaction 1.7 is the product of sodium-air reaction and accounts for the presence of oxygen in the carbon block (23)

He also detected the presence of NaF crystals at the carbon cathode/cast iron interface. This compound was believed to be the product of the reaction 1.9. It was not emphasized whether NaF diffuses into the cast iron or not. It was stated that depending on the temperature, NaF can percolate away from the reaction site. He also added that Na diffuses into the cast iron through graphite flakes. The carburization of the steel was also reported. The source of the carbon was claimed to be the carbon block. Based on these findings he concluded that a progressive (quantity was not given) increase in cathode voltage drop occurs during the operation.

The carburization of the steel encased directly in the carbon block was attributed to the presence of the free sodium (30). Na was suspected to promote the carbon diffusion from the block into the steel. Haupin (31) reported that the voltage drop at the carbon/collector bar interface increases during operation. This increase was estimated to represent 3% of the overall energy input during the entire lifetime of the cell.

Recently it was shown that high phosphorous gray cast iron, used as state of the art sealing material, poses a reduction in electrical conductivity (32). They articulated that because phosphorous is present as a chemical compound (we will show in 'Discussions' that this is Fe_3P of the ternary eutectic) it cannot diffuse as rapidly as the elements and aligns as an insulating layer that is parallel to the cast iron/steel interface. They stated that this alignment is a contributing factor to the increased voltage drop within the rodding. They also suggested the use of ferritic ductile iron with low phosphorous content as the rodding material.

It should be stressed out that there is little information in the literature about the carbon/cast iron/collector bar interfaces. However in order to provide a fair discussion, in the 'Discussions' section, we refer to the articles published in closely related fields such as diffusion bonding of cast iron to steel, microstructure development in cast irons and steels, effect of the magnetic field on the metallurgy of cast irons and steels, *etc.*

2. SAMPLE PREPARATION

2.1. Introduction

The collector bars and surrounding cast iron (compositions are given in Table 2.1) extracted from the center of the cells (Figure 2.1) provided by the HYDRO aluminum constitute the main part of this thesis as its interaction with the surroundings plays a key role in determining the electrical resistance. Hence, a proper sampling of the bar was of crucial importance to assure an accurate analysis and form a solid understanding of the events occurring in its interior and surroundings. Investigation of the bar/cast iron interface involves the consideration of both the side and the top interfaces as the course of the diffusion might differ depending upon the direction and this might have an impact on the course of the reactions.

From here onwards we adopt a terminology where S1 and S2 (Figure 2.2 and Figure 2.3) represent 7-days-old and 2190-days-old (6 years) samples respectively. The collector bars were taken after the cells had been shut down and cooled down to room temperature. The proper selection of the saw is important for the sectioning the bar since it builds up a stress and may lead to the cast iron layer breaking away from the bar surface (the temperature is controlled by using water as the coolant. Therefore the effect of the temperature was disregarded). This happened in the first attempt which therefore guided us to employ the water-jet to maintain the cast iron intact at the bar surface. However water jet cutting caused peeling off the cast iron from the top of the bar as well (Figure 2.2-a and Figure 2.2-b).

Table 2.1: Initial compositions of cast iron and the steel bar

	C	**Si**	**P**	**Mn**	**S**	**N_2**
wt.% in cast iron	2.8-3.2	1.8-2.4	1.4-1.7	0.4-0.7	<0.06	-----
wt.% in steel bar	<0.060	<0.070	<0.030	<0.400	<0.040	<0.012

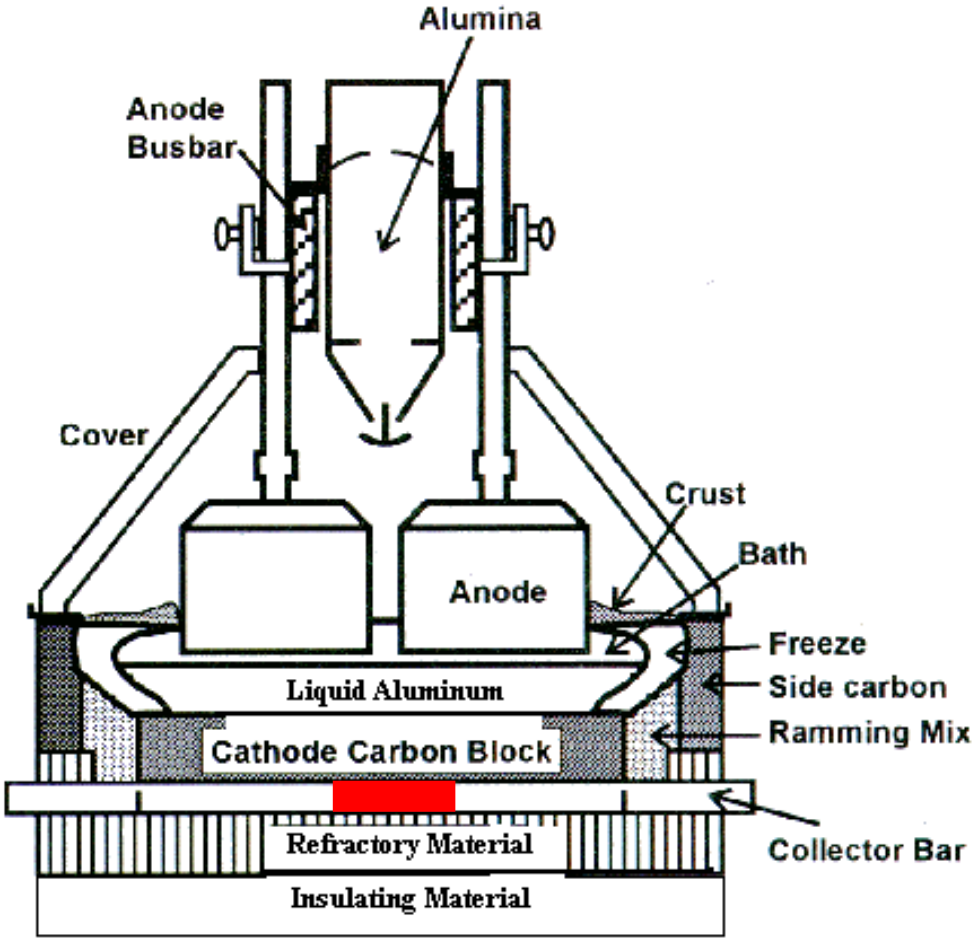

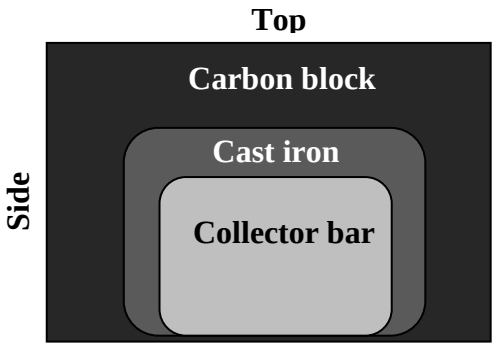

Figure 2.1: a) A reduction cell with a red rectangle indicating the area where the samples were taken **b)** Illustration of the cross section of the carbon/cast iron/steel interface.

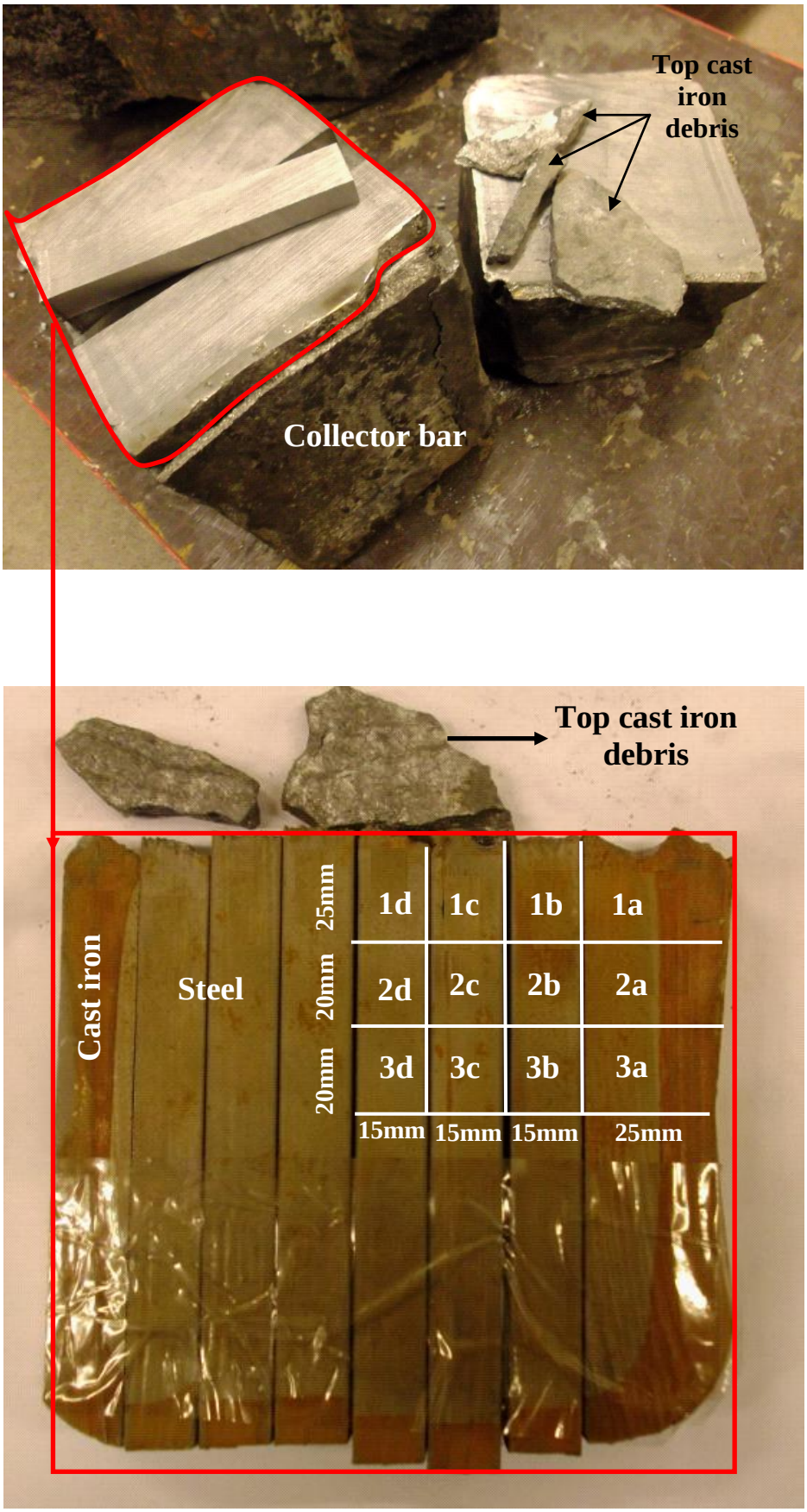

Figure 2.2: a) Collector bar (S1) after water jet cutting **b)** Sample numbering system

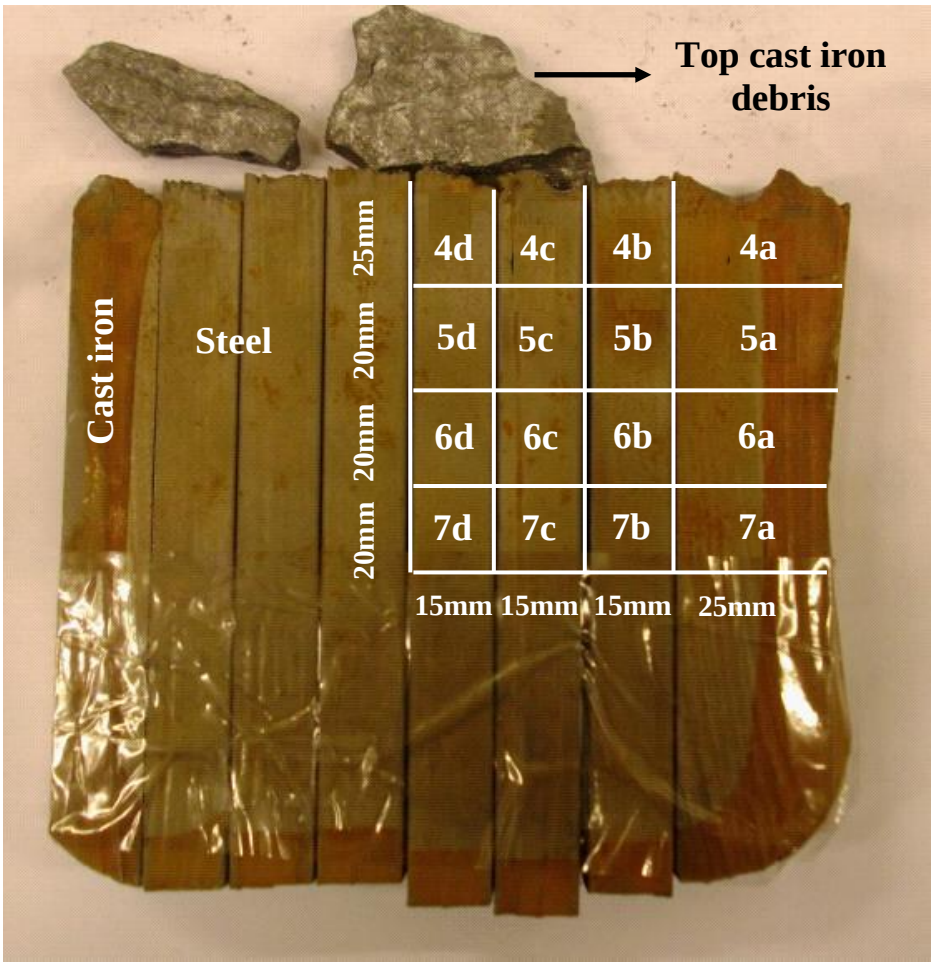

Figure 2.3: Sample numbering system of the sample S2

After obtaining the manageable and smaller sized specimens from the parent material using water jet, SiC circular saw was used for final tailoring of the sample. Only upper right quarter of the cross section of the bars was investigated (upper left is identical to the upper right and the interaction of the bar with the refractory layer at the bottom was not within the scope of the thesis). The dimensions of the specimens are given in Figure 2.2-b and Figure 2.3. The sample seen in Figure 2.2 was taken from the bar that was in operation for 7 days (S1). The other sample (S2) was extracted from a cell shut down after 2190 days (6 years) in operation and the main focus will be given to its microstructure throughout the thesis.

Column 'd' samples are equal distance from the sides of the bar to mitigate the intervention of diffusing species from the sides and model the diffusion dictated primarily by the downward direction. The same procedure was performed for the samples in row '3'. That is, they are positioned at equal distance to the top and the bottom of the bar.

2.2. Grinding and Polishing

2.2.1. General Principles and Experimental Procedure

Metallographic examination is done to classify the phases present in the microstructure of the materials according to their shape, size and distribution (33) and pinpoint the reasons for failure. The most important steps of metallographic sample preparation are grinding and polishing, because the final surface is shaped through these steps. The grinding and ensuing polishing is required to smoothen the surface and eliminate the damage made by cutting tool with an ultimate goal of providing excellent reflectivity. Grinding can be done either by automated machines or by hand using various grinding papers of different grids on a horizontal rotary grinding wheel (see Appendices A1 (34)). Of the commercial abrasive grains, the most common ones are silicon carbide (SiC) and aluminum oxide, Al_2O_3.

Each grinding paper produces its own damage, while removing the damage of preceding paper. The depth of the damage reduces as the grid number increases and depends on the materials type, that is, depth introduced is greater with soft materials than that with hard materials for a given grid size. Hand grinding is a tough task that may lead to unsuccessful surface conditions for both optical and electron microscope investigations. Improperly exerted force on the sample will result in uneven surface (error of flatness) that will impede the

grinding of the sample and subsequently the removal of the scratches from the previous paper. A gently applied force will ease the handling of the process and give a satisfactorily flat and mirror-like surface. Another point that deserves a passing mention is that the sample should be rotated by an angle of 90^0 between each grinding. The holding time at each grinding paper should be twice the time spent until the scratches from previous paper have been completely removed. If there are pertinent scratches, this may be originated from either uneven surface or overused paper. Among the measures for ameliorating of this problem are employing a new paper. If it does not solve the problem, then it is wise to switch to the preceding paper (or smaller grid papers) and start over grinding until the surface becomes flattened.

We figured that manual method of wet-grinding (water) was satisfactory for our purpose and followed a sequence of grinding with 320 grit through 2400 grit that was ensued by polishing process with diamond powders of 3μ and 1μ respectively, with the aid of a lubricant present. Between each grinding paper, the sample was washed thoroughly with water in order to remove the remaining particles from the previous paper. When the grinding was completed the samples were immersed down in ultrasonic vibration system filled with ethanol to ensure an ultra-clean surface (the main thrust here is to ensure the complete removal of micro-particles clinging to holes/cracks) for a satisfactory performance at the polishing step.

Some alloys, when examined with optical microscope, allow phase identification of the sample by means of reflectance differences, such as graphite in cast iron (35). However, revealing the microstructures like pearlite, etching of the sample is necessary. Etching is a process where the different response rates of different phases in the sample to the etchant is utilized to create a contrast under the optical microscope. The metallographers, in case they have access to SEM facilities, sometimes do not require etching process (SEM creates contrasts between different phases according to the chemical composition). It is highly recommended to the researchers to prepare their samples in such a way that will permit the use of optical microscope in phase identification as the SEM is time and cost prohibitive. Because the microstructures encountered in steels are not distinguishable by SEM without etching, although we extensively utilized the SEM, we applied an etchant (2%Nital) to our samples so as to enable us to see the microstructure properly.

2.3. Analytical Instruments Used

2.3.1. Scanning Electron Microscope (SEM) and Energy Dispersive X-ray Spectroscopy (EDX)

SEM is an analytical instrument that irradiates the material to be sample with a focused electron beam. As the electron beam impinges on the sample, the sample emits secondary electrons, characteristic X-rays, backscatter electrons, Auger electrons and photons with various energies (36). The signals from these emissions are then collected by a detector and used to produce high resolution images. The most used signals in SEM are backscatter and secondary electrons. Energy dispersive X-ray spectroscopy is a chemical microanalysis technique. It is used in combination with SEM (37). It provides information about the chemical composition of the sample by analyzing the relative abundance of the emitted X-rays.

3. RESULTS

3.1. Introduction

In order to provide a complete picture of the bar/cast iron microstructure, all the samples were investigated with light microscope individually and the individual images were combined to illustrate the entire cross sections. Figure 3.1 represents the optical micrographs of the entire cross section of S1 and S2. As the upper right section of the figure corresponds to the top/side transition where the material was under the influence of the diffusion both from the top and the side, the evaluation of the diffusion path and the consequent microstructural evolution is constrained.

The images in column '4' present the microstructure of the cast iron on the side of the bar. It is seen that from top to bottom the microstructure is composed of temper graphite dispersed in a ferritic matrix. The size and the shape of the temper graphite are consistent with each other downstream and the size decreases further to the left. In the images in column '3', there is a sudden change observed in the microstructure of the matrix from ferrite to pearlite (see Appendix-B for the metallurgy of cast irons and steels). In all the images in column '3', the interface line that represents the ferrite/pearlite transition occurs at a distance from the side in decreasing order downstream. Another interface line manifests itself with a black line in the images in column '3' in S1 and column '2' in S2, which we attribute to the initial cast iron/bar interface (see discussions). In 'T1' and 'T2', top images show a horizontal interface separating columnar ferrite region from the pearlite region. These horizontal interfaces will be discussed adapting both "temperature gradient and magnetic field" approach in the discussion section which we did not set out to involve in the beginning.

Figure 3.1-a represents the entire surface of S1 undertaken with light microscope. The most notable difference from S2 seems to be the ferritic center of the bar (M1) which indicates that

the carbon concentration in the center of the bar could not reach the level to which S2 did (columns '1,2 and half of the 3' in S2 are composed of pearlite). Another prominent difference is the more marked interface labeled by a vertical black line in column '3'. This interface is the equivalence to that found in S2 in column '2'.

It should be noted that although each individual pictures are given in the same length scale, they do not necessarily indicate their exact distance from the top or sidewalls. For example, right end of the sample L3 was not adjacent to the left end of the sample L4. That is, all individual images are the microstructural representatives of the region they were extracted from. Another clarifying example is that although the vertical black lines in S1 and S2 are positioned in column '3' and '2' respectively, they actually are at the same distance from the side of S1 and S2. It should also be noted that the images in columns '2', '3', '4', for instance, represent only samples in column 'a' in Figure 2.2-b and Figure 2.3; because the samples in column 'b', 'c' and 'd' are identical to the left end area of the images in column 'a' with regard to their microstructures.

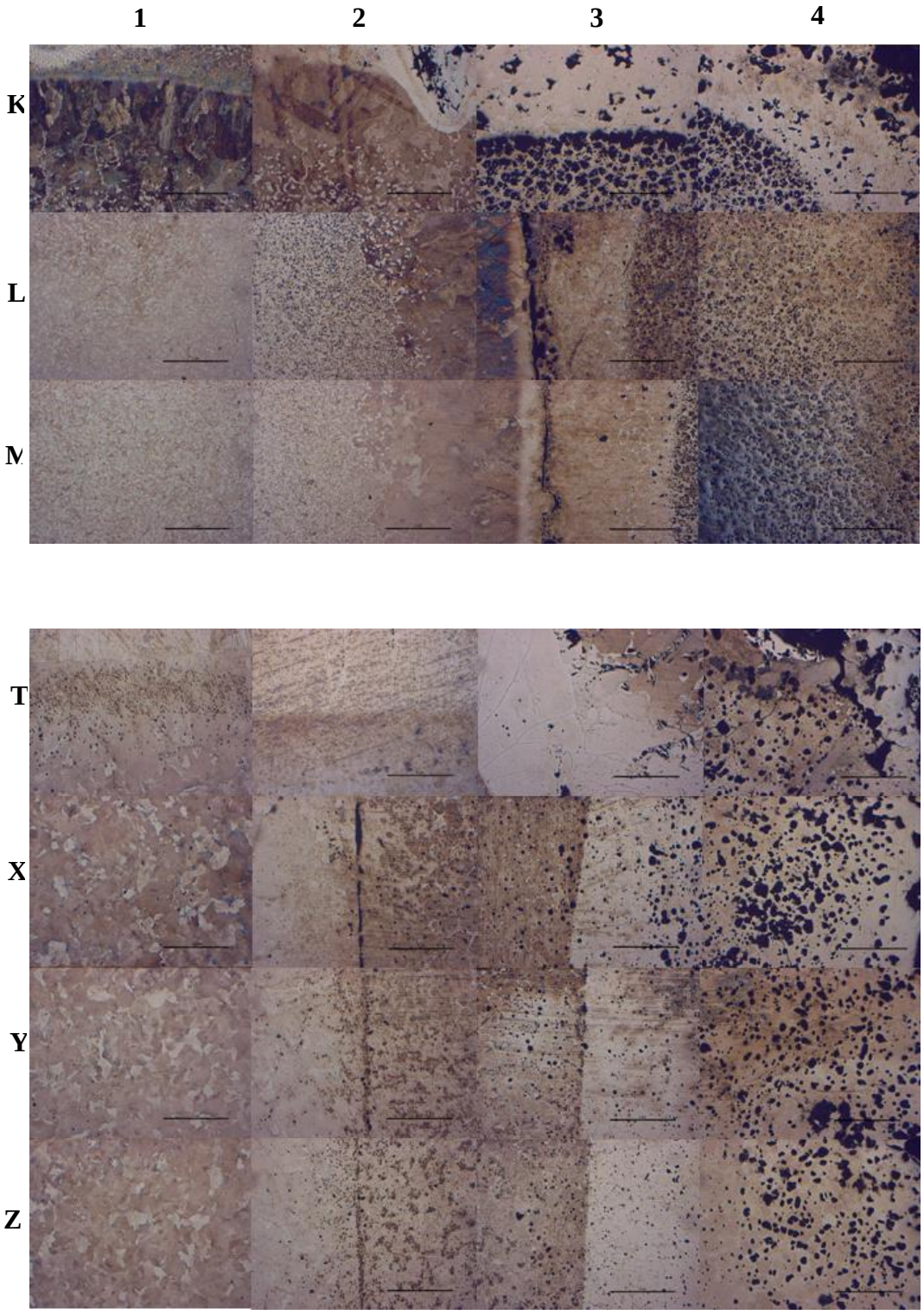

Figure 3.1: A series of optic micrographs combined to illustrate the entire surface of **a)**S1 **b)**S2.

3.2. Side Analysis

To clearly depict the microstructures and respective elemental distributions, SEM/EDX analysis were performed with the samples in column 'd' and rows '3' and '6'. The logic behind this selection was that column 'd' was considered to show a microstructure affected dominantly by downstream diffusion while rows '3' and '6', was expected to reflect the effect of the horizontal diffusion from the sidewall. Hence we were able to develop a diffusion profile from both top and side to the interior of the bar.

SEM micrograph of section 6a is given in Figure 3.2. The chemical composition of respective phases is tabulated in Table 3.1. Upon acquisition of the composition over the whole sample, aluminum metal was identified by EDX system. As can be seen in the Table 3.1, while the sample contains aluminum even at its interior, it contains sodium metal only close to the sidewall. Therefore, in order to estimate the diffusion pathways for aluminum and sodium from the carbon block into the cast iron element maps were plotted using EDX system. The element map of 6a is given in Figure 3.3. In order to see the beginning of the evolution of the microstructure of the side cast iron and compare to S2, SEM micrograph and the element mapping of the section 3a is presented in Figure 3.4 and Figure 3.5 respectively.

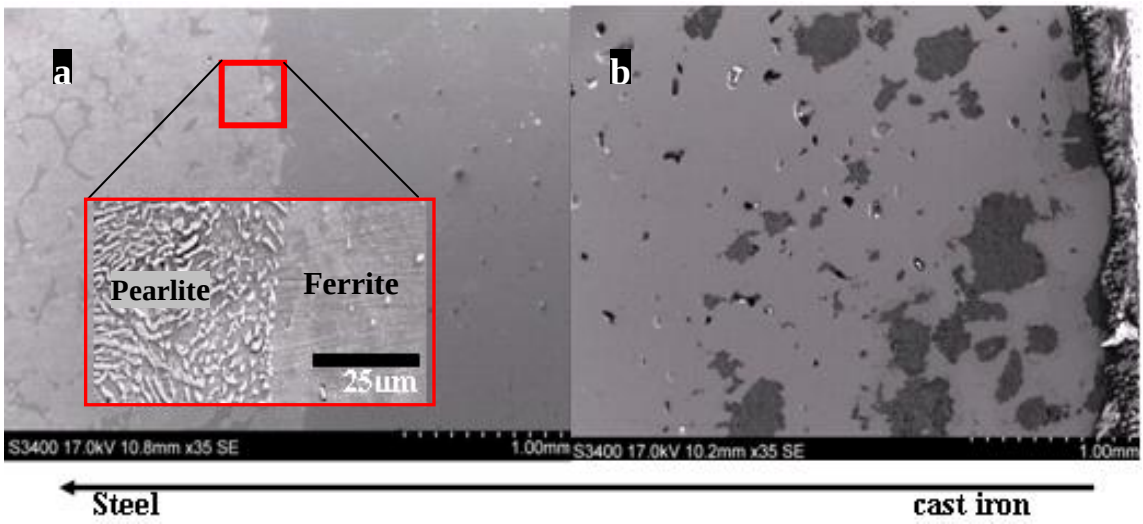

Figure 3.2: SEM micrographs of the sample 6a **a)** interior **b)** close to sidewall

Table 3.1: EDX results for ferrite in b, ferrite and pearlite in a and overall composition of b

Element	b (Ferritic Matrix)	b (overall)	a (Ferrite)	a (Pearlite)
C	3.42	6.86	3.40	4.65
O	0.13	5.32	0.01	0.41
F	1.93	2.51	2.05	2.06
Na	-----	1.38	-----	-----
Al	7.06	14.40	4.22	0.95
Si	1.57	1.06	1.59	1.51
P	0.55	0.36	1.84	0.39
S	0.01	-----	0.03	0.08
Ca	0.03	0.27	0.05	0.03
Mn	0.31	0.40	0.52	0.52
Fe	84.99	67.45	86.29	89.40
Total:	**100.00**	**100.00**	**100.00**	**100.00**

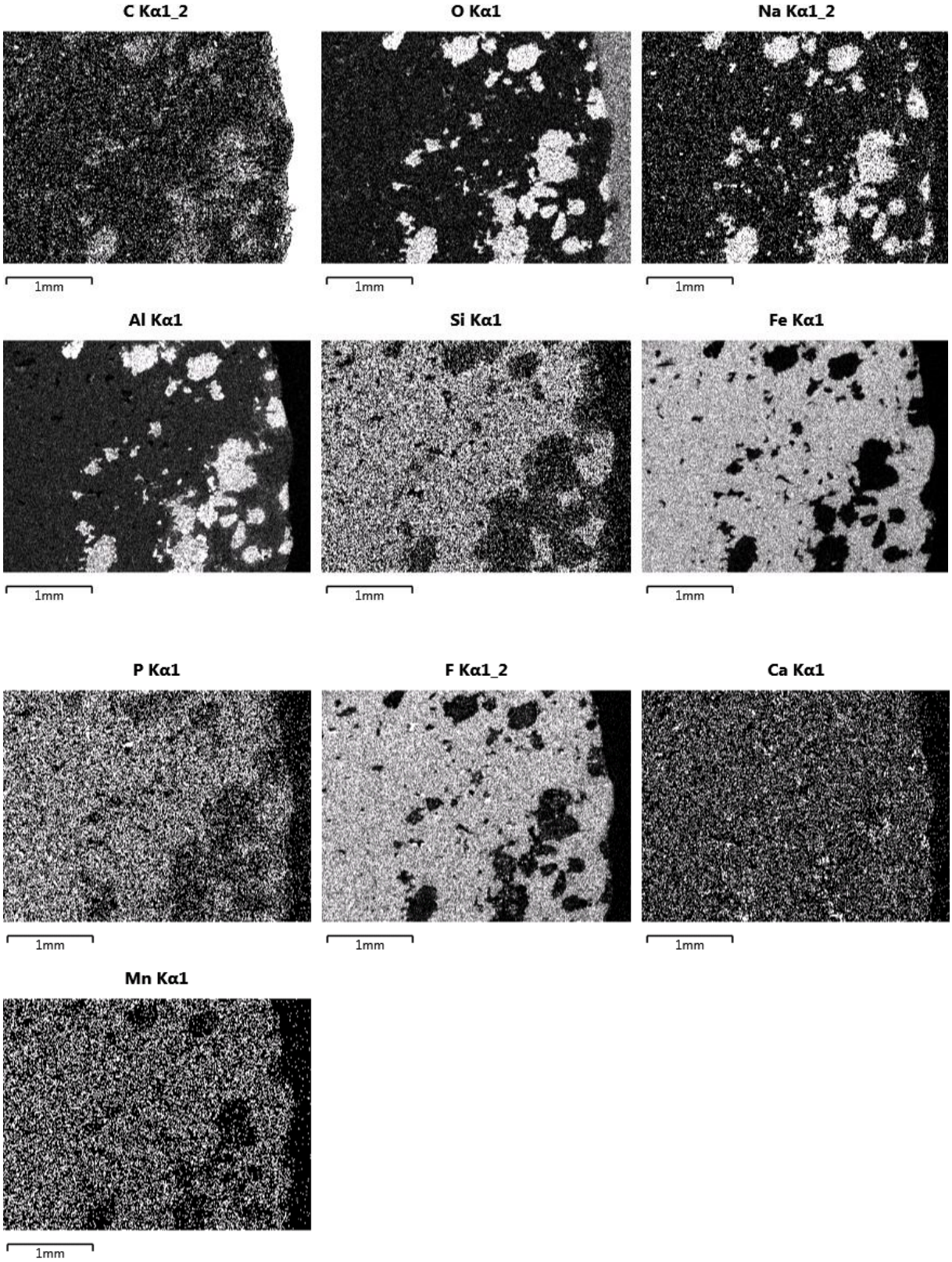

Figure 3.3: Element map of the region in Figure 3.2-b showing the aluminum, sodium and oxygen cumulating on the graphite.

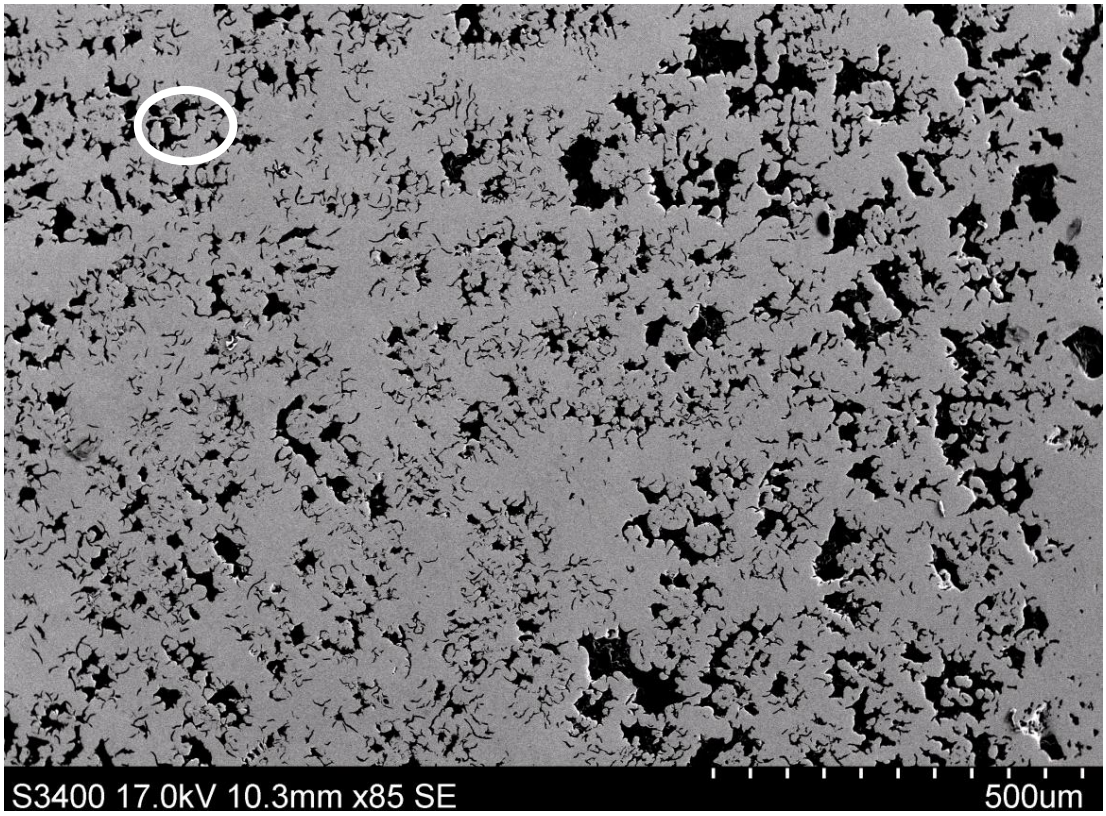

Figure 3.4: SEM micrograph of the cast iron region in the sample 3a

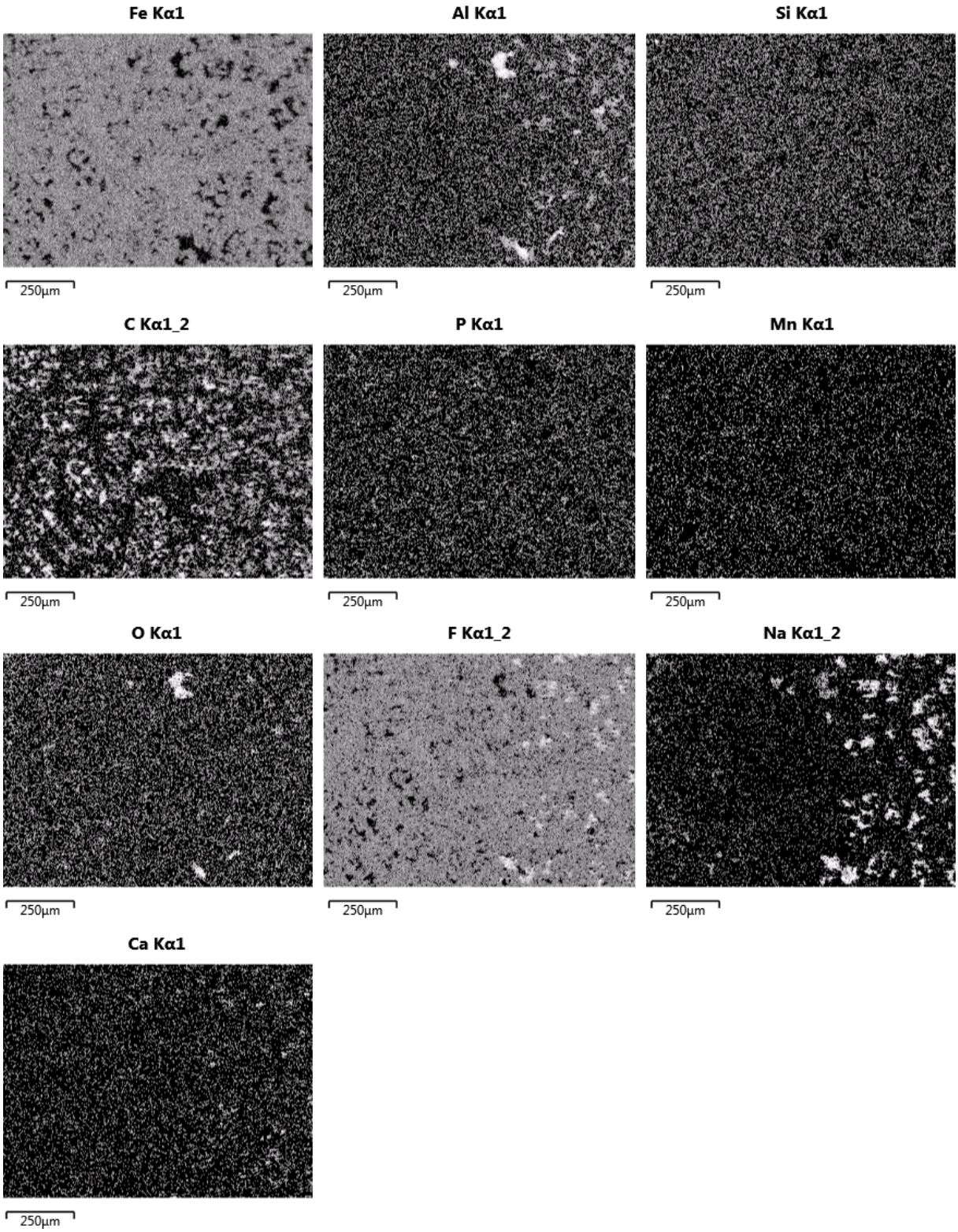

Figure 3.5: Element mapping for the sample given in Figure 3.4

Higher magnification SEM image of one of the temper graphite in 6a taken for further examination is given in Figure 3.6. Corresponding composition is tabulated in Table 3.2. The composition of graphite shows a high content of sodium, aluminum and oxygen. This finding helps us answer the question as to how aluminum and sodium enter the cast iron and the steel bar (only aluminum in steel). Additionally, as the scope of this thesis is confined to determining the contributing factors to the reduced electrical conductivity at block/cast iron/bar interface and as alloying the steel and cast iron with these elements reduces the conductivity, detection of these elements is a crucial finding for the outcomes of this thesis.

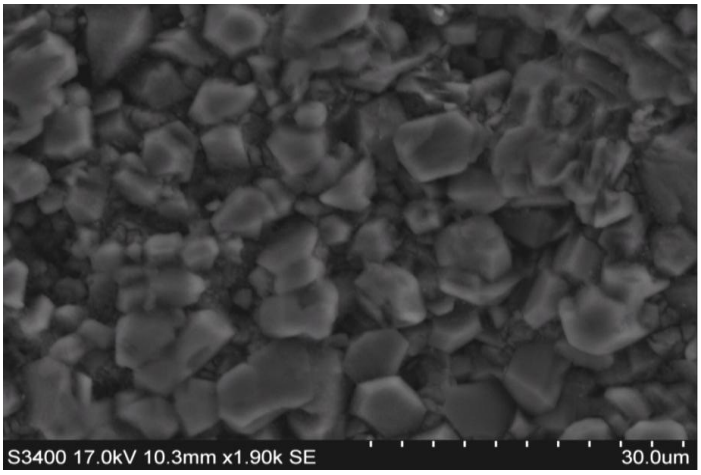

Figure 3.6: SEM micrograph of graphite in 6a

Table 3.2: EDX analysis of the graphite given in Figure 3.6

Element	Wt%
C	17.98
O	35.20
F	5.44
Na	3.95
Al	33.41
Si	0.36
Ca	1.15
Fe	2.51
Total:	**100.00**

However we considered Figure 3.6 insufficient to clearly depict how aluminum and sodium entered the graphite in the first place. To elucidate further we examined the graphite in 3a with SEM (Figure 3.7). Figure 3.7 gives an encompassing view into the temper graphite formation.

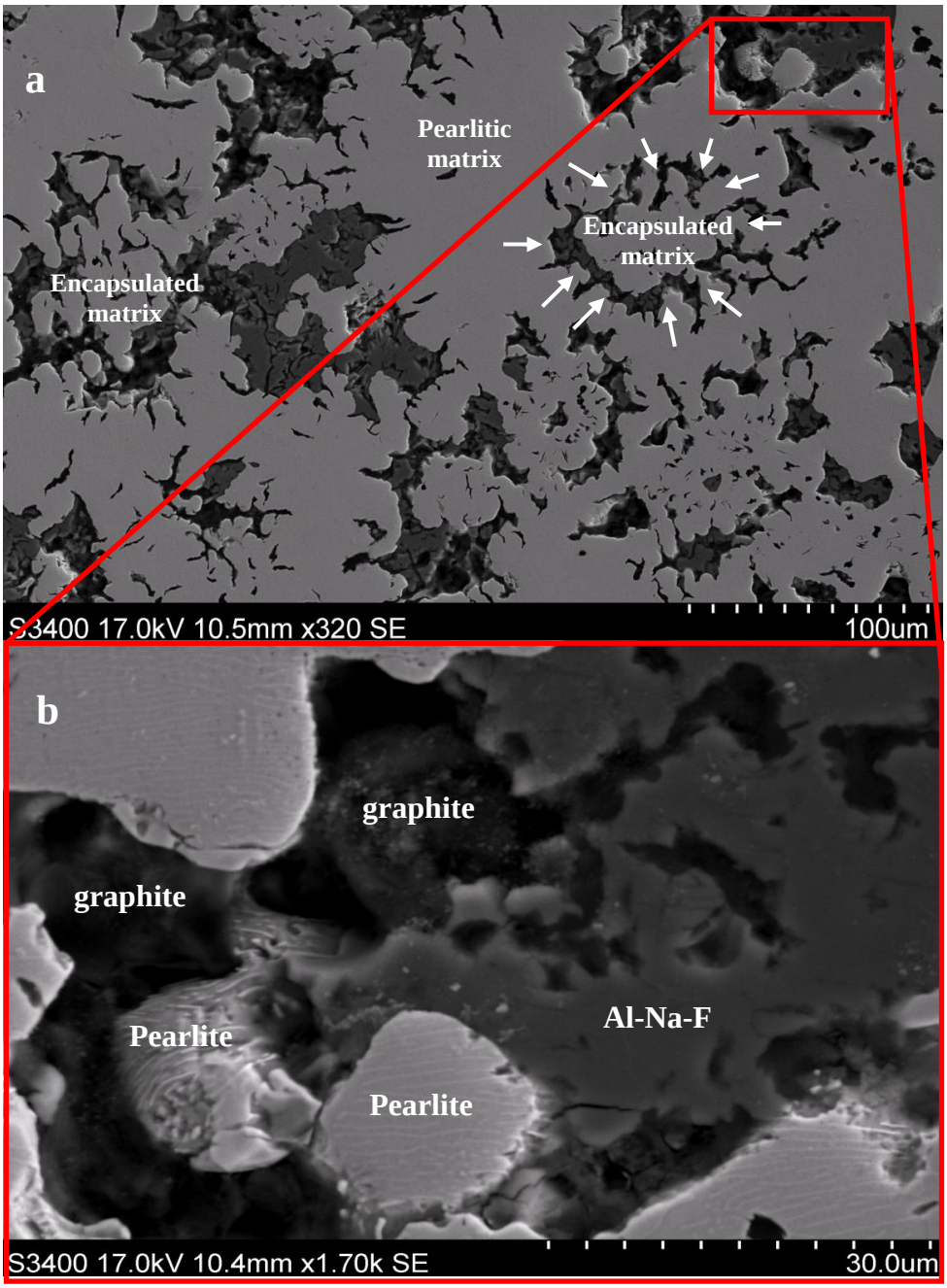

Figure 3.7: The SEM micrograph of section 3a in S1 **a)** Low magnification. White arrows indicate the graphite flakes forming encapsulating spheres **b)** High magnification

From the Figure 3.7 it is obvious that there are two distinct phases in the graphite, one is pitch black while the other appears dark gray. To distinguish these phases, element mapping was achieved with SEM (Figure 3.8) identifying the pitch black as graphite, while the dark grey phase was determined to be cumulated by sodium, aluminum and fluorine.

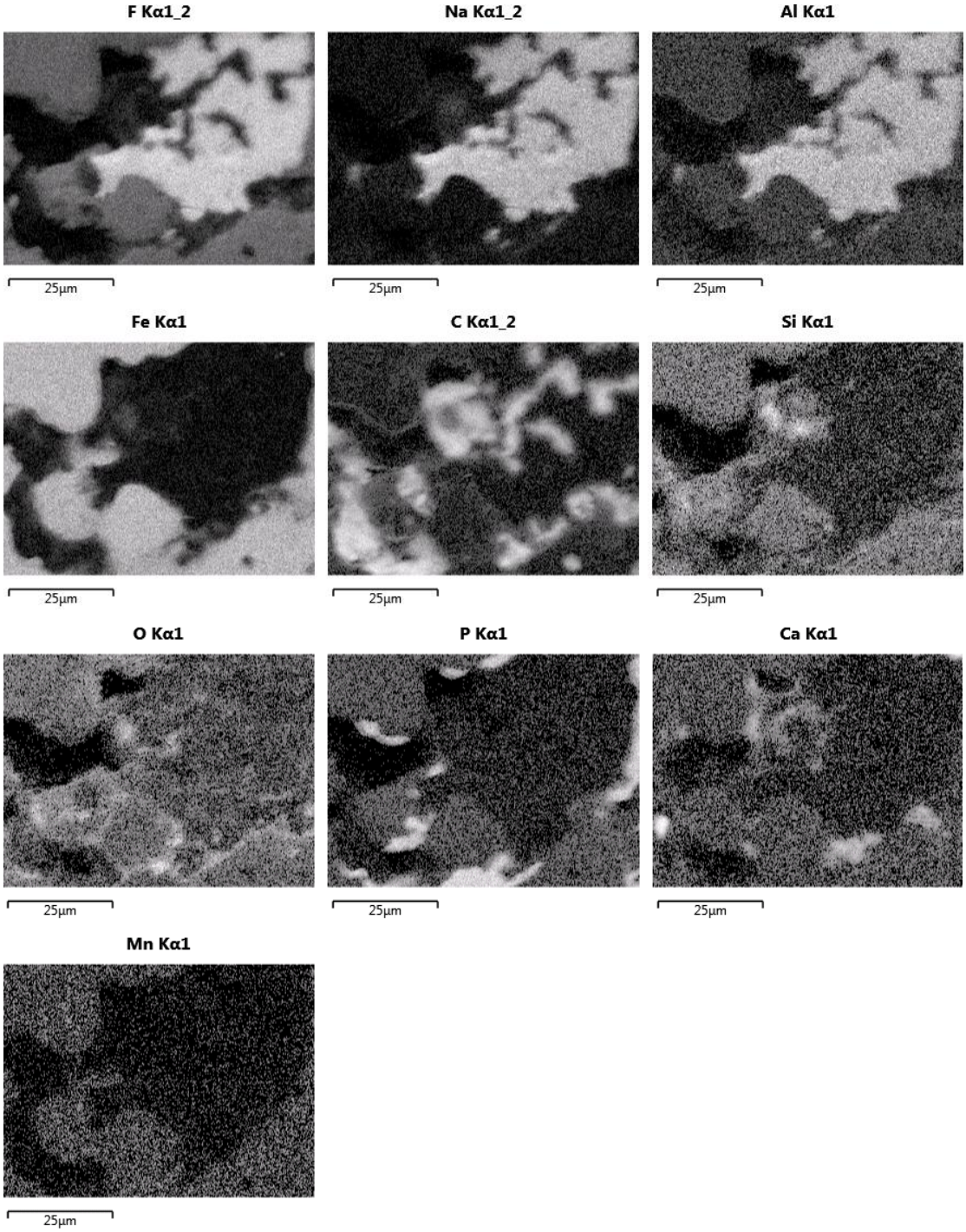

Figure 3.8: Element mapping for the region given in Figure 3.7-b.

The element map presented in Figure 3.8 provides many important findings. The most important one appears to be the pearlite islands surrounded by the graphite matrix. This may be summarizing the temper graphite formation. Furthermore the shape of P rich phase resembles that of ternary phosphide eutectic at the eutectic grain boundaries (See the discussions).

Another graphite particle deeper into the cast iron in 3a was also investigated with SEM (Figure 3.9-a) and an element map (Figure 3.9-b) was produced with EDX revealing neither aluminum nor sodium accumulation in the graphite (see Appendix-A2 for the chemical analysis of the surrounding matrix) .

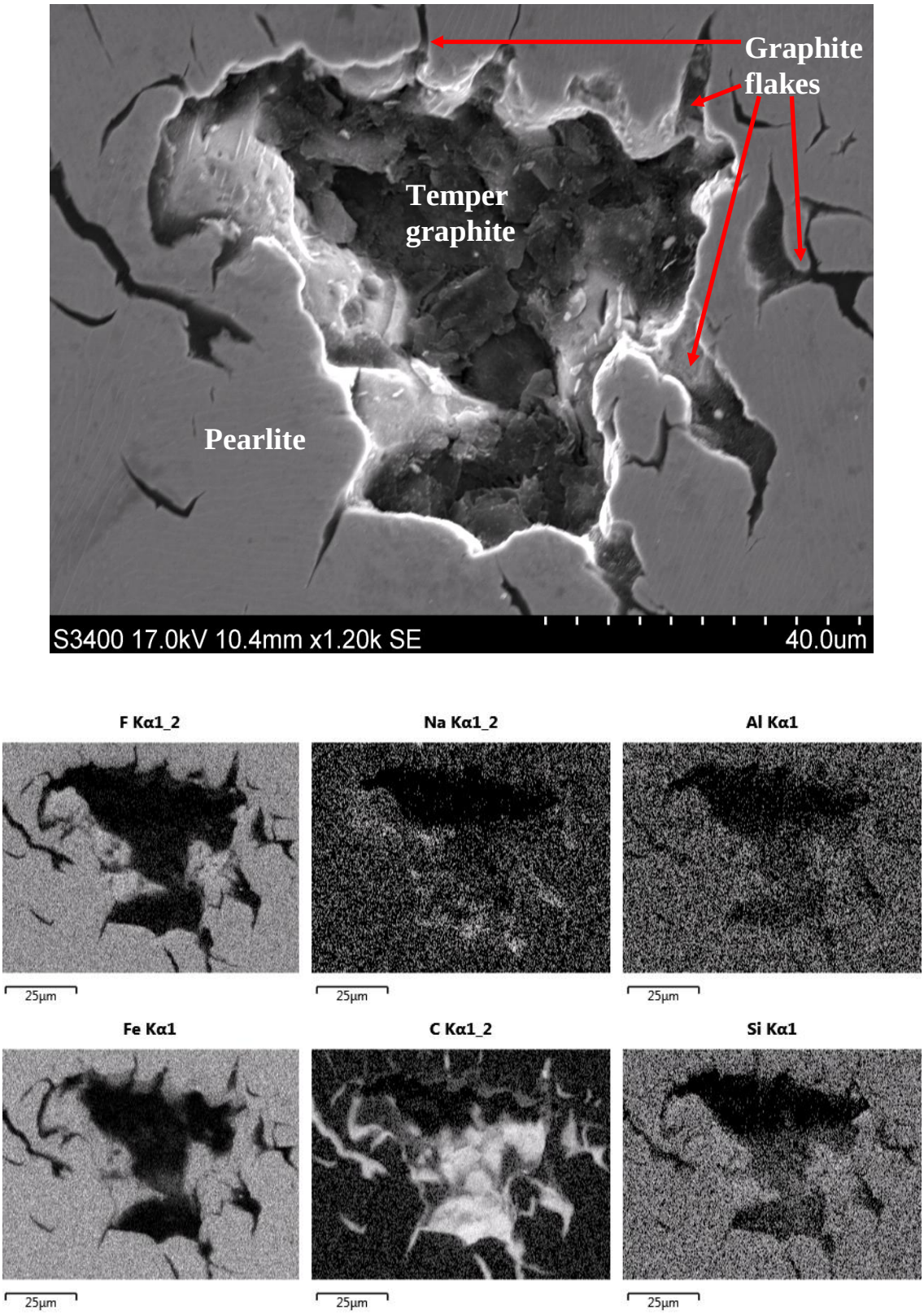

Figure 3.9: a)SEM micrograph of a temper graphite (taken from within the red circle in Figure 3.4) showing its growth by the incorporation of flake graphites **b)** Corresponding element mapping

Figure 3.10-a shows the further magnification SEM image of the outermost layer of the sample 6a. This layer was in direct contact with the carbon block during operation. A crack is clearly seen parallel to the interface. The element map plotted for the region surrounding the crack is presented in Figure 3.10-b. Determining whether the dark phase on the right side of the crack is graphite or cast iron posed difficulties but the presence of Si in it was assumed to be a good indicator that it is cast iron. As the crack reduces the contact surface area with consequent alteration of electrical conductivity, this finding may be helpful in explaining the CVD in cathode assembly (see Appendix A-3 for additional SEM images showing the crack).

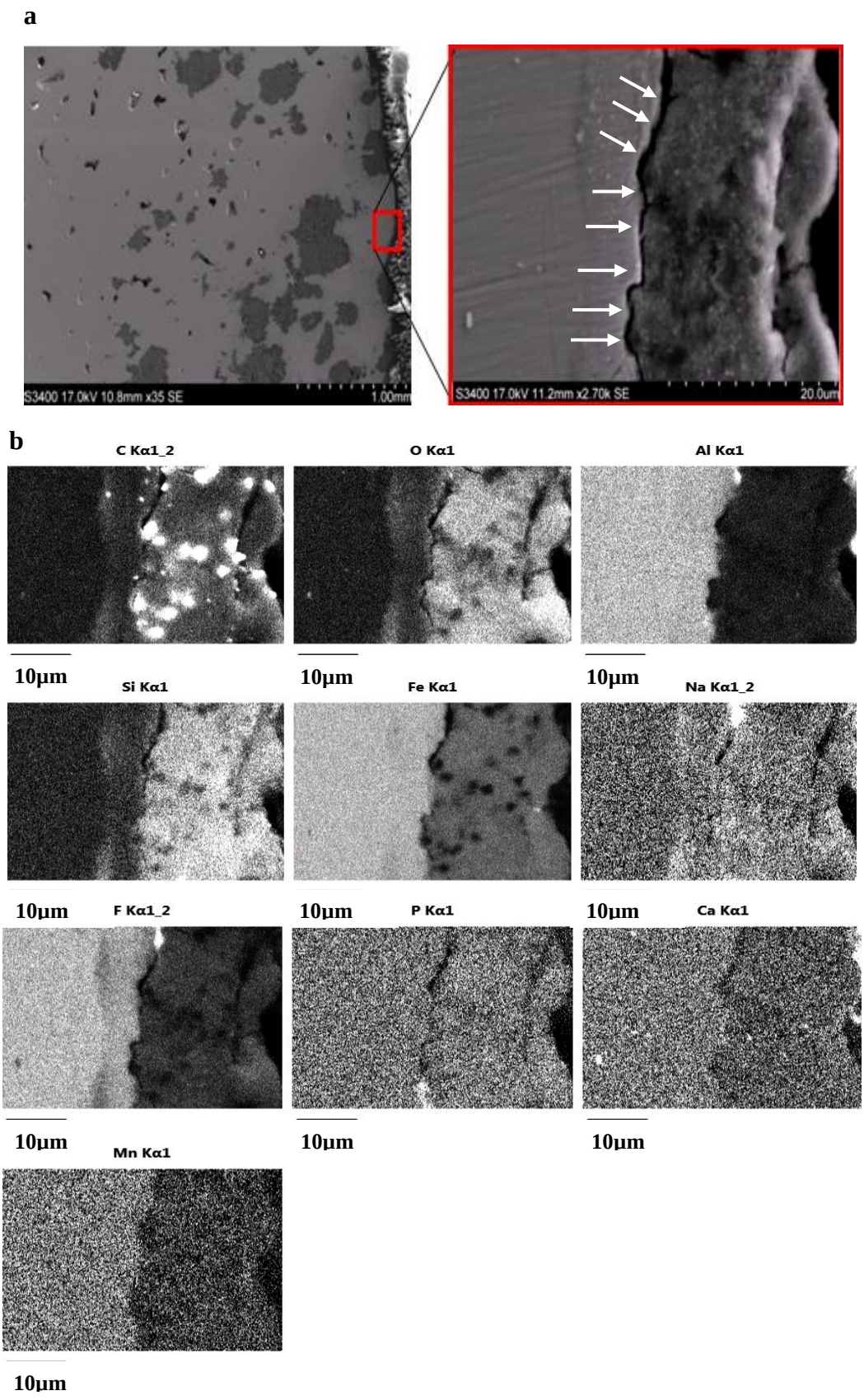

Figure 3.10: a) SEM micrograph of cast iron/block interface of sample 6a with arrows pointing the crack line **b)** Corresponding element map

3.3. Top Analysis

The top surface analysis was performed with the sample 4d because it was located midway between the sides of the bar and thus expected to exhibit a behavior dictated primarily by the downstream material flux. The optic micrograph with increased magnification of 4d and the corresponding element map is given in Figure 3.11 and Figure 3.12 respectively. As can be clearly seen in the Figure 3.11, upper layer of the sample is composed entirely of columnar ferrite grains. On top of the columnar grains is a phosphorous rich layer as identified by EDX analysis (It should be noted that the images might have been taken from slightly different regions on the same sample as two different microscope were used). The chemical composition of phosphorous rich top layer is given in Table 3.3. It indicates the formation of an Fe-P compound that preferentially settles down at the grain boundaries. We also wanted to see to what extent this compound goes down into the cast iron. The element map of only P at columnar ferrite/pearlite transition in 4d is given in Figure 3.13. It is seen that Fe-P compound no longer exists below the interface.

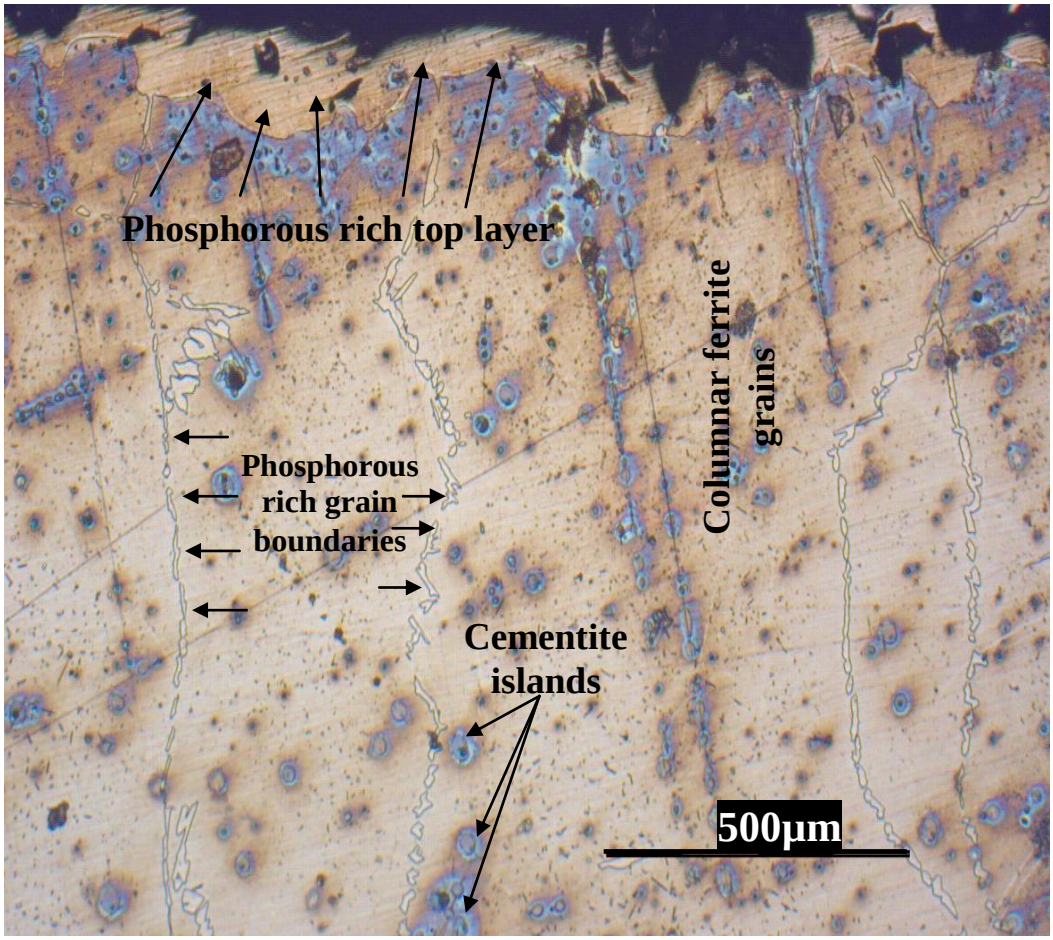

Figure 3.11: Optic micrograph of the top layer taken from the sample 4d showing the phosphorous rich top layer and grain boundaries. It should be noted that some of the nodular islands represent cementite, while some represent small nodular graphite.

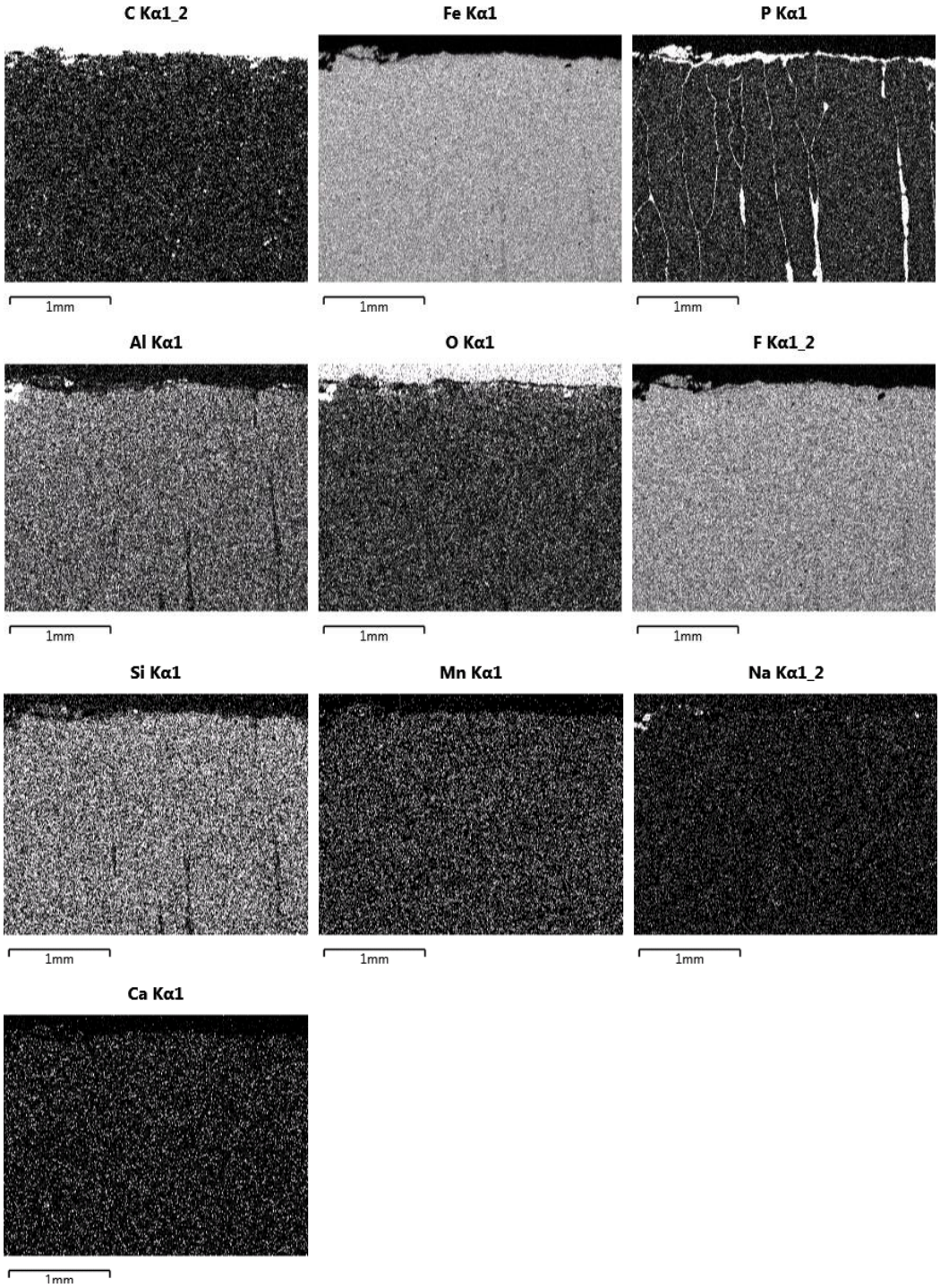

Figure 3.12: Element map of the sample given in Figure 3.11

Table 3.3: EDX analysis of phosphorous rich layer on top of sample 4d

Element	Wt%
C	5.20
Al	0.44
F	2.44
Mn	0.53
P	12.93
Fe	78.46
Total:	**100.00**

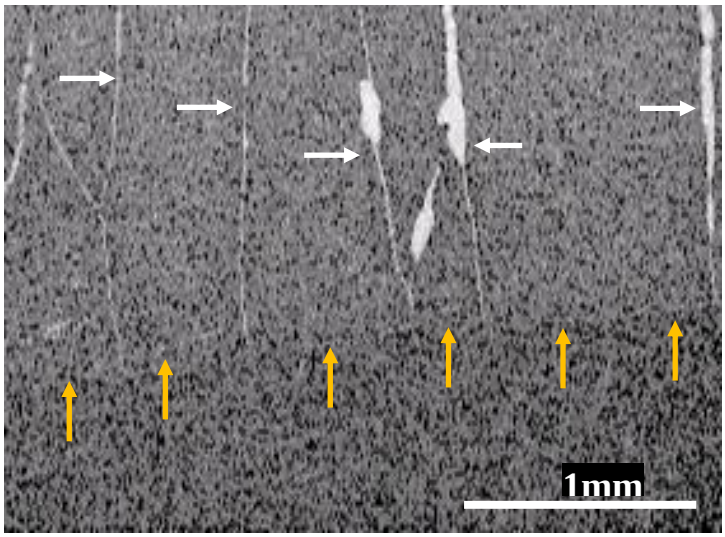

Figure 3.13: Element map of P at columnar ferrite/pearlite transition in 4d. Red arrows point the grain boundaries of columnar ferrite grains while the yellow ones indicate the ferrite/pearlite interface.

3.4. Analysis of the Debris

As already mentioned in the sample preparation section, the cast iron layer on top of the bar was peeled of during the sample preparation with water jet. The debris from the top cast iron layer was examined with SEM (Figure 3.14-a) and optical microscope (Figure 3.14-b) and element mapping was constructed (Figure 3.15) for the same layer. Its chemical content was identified by EDX analysis and is given in Table 3.4. It should be emphasized that the cast iron layer on top of the bar differs from that on the side with regards to distribution of sodium, aluminum, oxygen and fluorine. The occurrence of sodium and fluorine at the same pixel may indicate NaF. Furthermore, EDX did not detect any phosphorous in the debris.

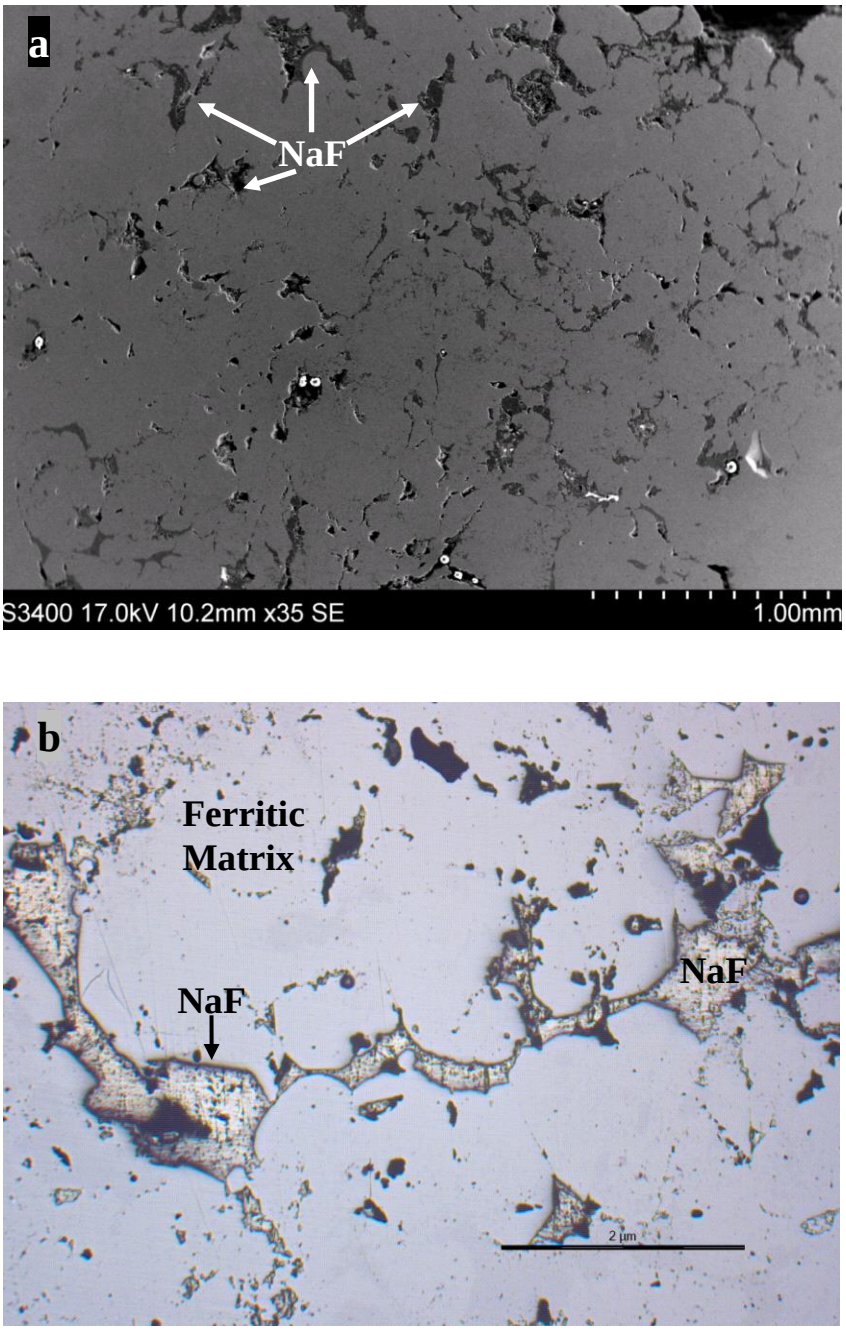

Figure 3.14: Micrographs of top cast iron debris **a)** SEM **b)** Optic microscope

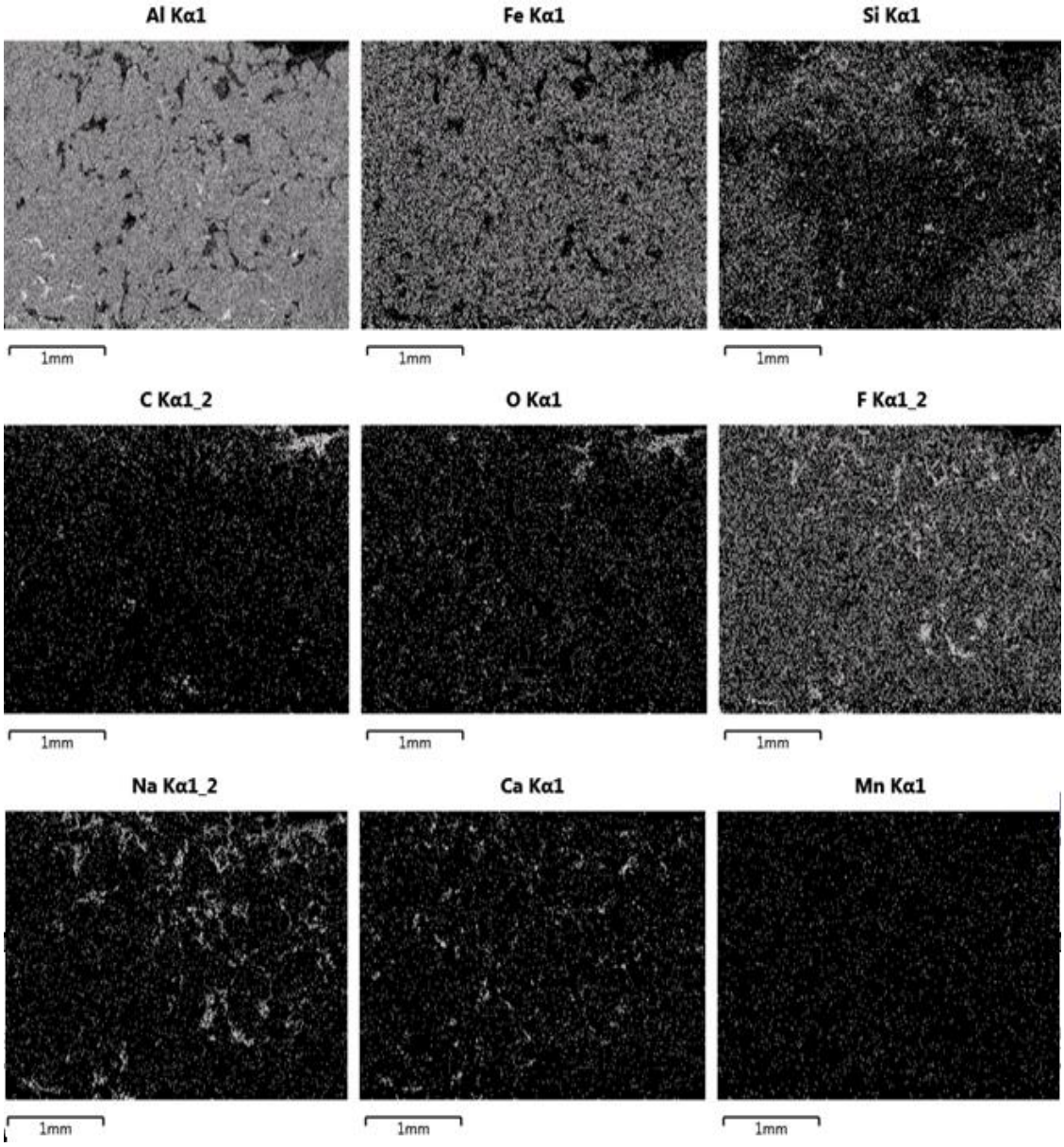

Figure 3.15: Element map of the debris from the top cast iron layer. Since the layer was crashed during sampling, the exact location of the sample is not certain. Note that Na map overlaps that of F indicating NaF. The Ca enrichment on the same spots also suggests bath penetration.

It should be noted that although S appears among the constituents, element map does not show it. This is simply because, it amounts too little and the dwell time (secondary electron detector) is not enough to identify it. It is surprising that aluminum predominates on iron in cast iron, because it is not among the alloying elements and comes from the bath or the liquid metal pad on the cathode surface.

Table 3.4: Chemical composition of the debris from the top cast iron layer

Element	**Wt%**
C	13.25
O	2.30
F	4.40
Na	1.22
Al	46.48
Si	3.65
S	0.04
Ca	0.58
Mn	0.29
Fe	27.79
Total:	**100.00**

4. DISCUSSION

4.1. Side analysis

The first SEM/EDX and optical microscopy analysis was performed with 6a taken from the side bar/cast iron interface in S2. Both macroscopic and microscopic approach was deployed to develop a complete vision of the compositional variations throughout the sample. Figure 3.1 presents the optical micrographs of the samples that allow us to unambiguously identify the layers present throughout the entire cross section of S1 and S2. It was expected not easy to accurately pinpoint the interface since the sample was in service for 6 years at the operating temperatures of ~ 900-950^{0}C which should have resulted in both substantial bonding of cast iron to steel through solid state diffusion bonding and crystallization of austenite at this temperature range that both must have diminished the interface line. However the layers of different microstructures given rise by varying carbon content across the cast iron and steel bar revealed distinguished features that might be utilized in pinpointing the approximate position of the interface and the carbon diffusion path.

Figure 3.2 highlights the microstructural changes from side (cast iron/carbon block) to the interior of the cast iron in S2. It shows a drastic change in the microstructure which manifests itself with an apparent interface line. This situation endorses us to pose the right question to clearly depict the formation mechanism of this interface; "How did the phases on the sides of this interface form?". It shows transition from typical temper graphite (heat treated malleable cast iron) embedded in a ferritic matrix to a fully pearlitic structure. Malleable cast iron implies that the cast iron solidified into white cast iron following the sealing process, because white cast iron is the precursor to producing temper graphite in ferritic matrix. As can be seen in Figure 3.2, no pearlite formation close to the side had occurred upon cooling below the eutectoid temperature as the cooling rate was sufficiently slow as to enable the remaining excess carbon to deposit onto the temper graphite that were already present (formed during the operation at 950^{0}C). The sequence of microstructural change from ferritic matrix into

pearlite can be explained by the fact that there is lower carbon solubility in ferrite than that in austenite (see Appendix-B, Figure B-1). Since a positive temperature gradient from side to the interior is established upon cooling, carbon that initially dissolved in austenite grains will be expelled when ferrite transformation begins at eutectoid temperature and start diffusing away from the side to the interior where the temperature is relatively high for austenite to linger. The migration of carbon from side to the interior can be corroborated by consulting another fact that carbon diffuses in ferrite at a higher rate than that in austenite (see Appendix-A4) which should result in a carbon rich layer at ferrite/pearlite interface (Austenite located deeper in the cast iron transforms into pearlite plus graphite upon cooling not into ferrite because the remaining austenite at the interior bears higher carbon). The reason for a ferrite/pearlite transition interface to form is that, when temperature reaches a value below than what is required to facilitate an effective diffusion, carbon diffusion is ceased. Figure 4.1-a shows this phenomena occurring in 5a (Figure 3.1-b column 3 shall also be referred in order to ensure a statistical judgment). Figure 4.1 is the larger view of X3 in Figure 3.1b.

The element map of P in Figure 4.1-b shows a phosphorous rich phase present at the grain boundaries. As we will discuss in the next section, this phase is in liquid form at operating temperatures. Having a liquid phase within the rodding during operation is detrimental for the contact pressure, which in turn increases the contact resistance at the interface (see Appendix-A5 for the volumetric change as a function of temperature). High phosphorous cast iron exhibits a dramatic drop in thermal dilatation at ~925^0C. This temperature corresponds to the melting point of Fe_3P (For details of this phase see the next section).

In Figure 3.1-b the images in column '2' present a vertical black line that should be representing the original cast iron/steel interface. This interface is more pronounced in S1. The SEM micrographs and corresponding element mapping of P at the interface of 3a and 6a are given in Figure 4.2. One should see that the bonding process has not been completed yet in 3a and interface is more pronounced than 6a. Encountering the original interface in S2 is intriguing because the operation life and temperature was enough to allow the austenite to crystallize that eventually would diminish the initial interface. Such a phenomenon previously was reported by various researchers (38, 39) even at experimental times as short as minutes to hours. The element mapping of P in Figure 4.2-d concludes that it is the cast iron/steel bar interface. Because, as shown by Majerova et.*al.* (40), the ternary phosphide eutectic is concave triangular in shape in cast iron, while in steels (low P content) this phase does not

form. The reason phosphorous is evenly distributed in 6a which does not allow us to pinpoint the interface, may be that the time was sufficient for phosphorous eutectic to diffuse into the steel. Because Fe_3P is a molecule, it can not readily diffuse as the elements do.

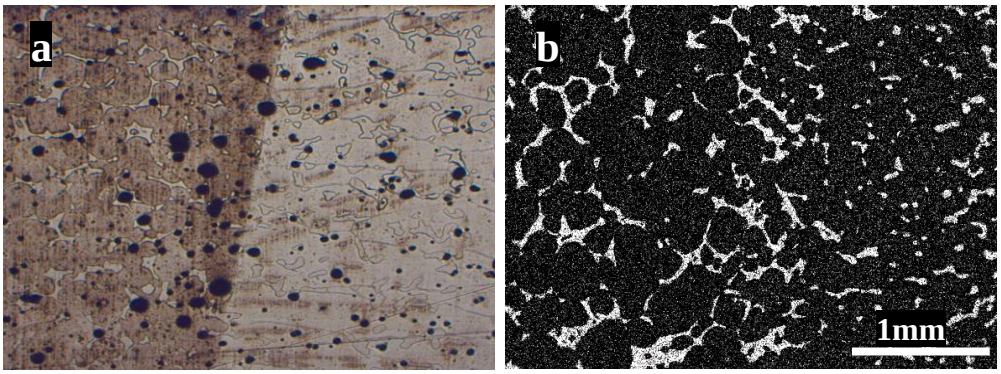

Figure 4.1: Ferrite/pearlite interface in 5b. **a)** SEM micrograph **b)** Element mapping for P. The temper graphite is larger in size on the left of the interface as C concentration increases locally due to its reduced diffusion rate in austenite.

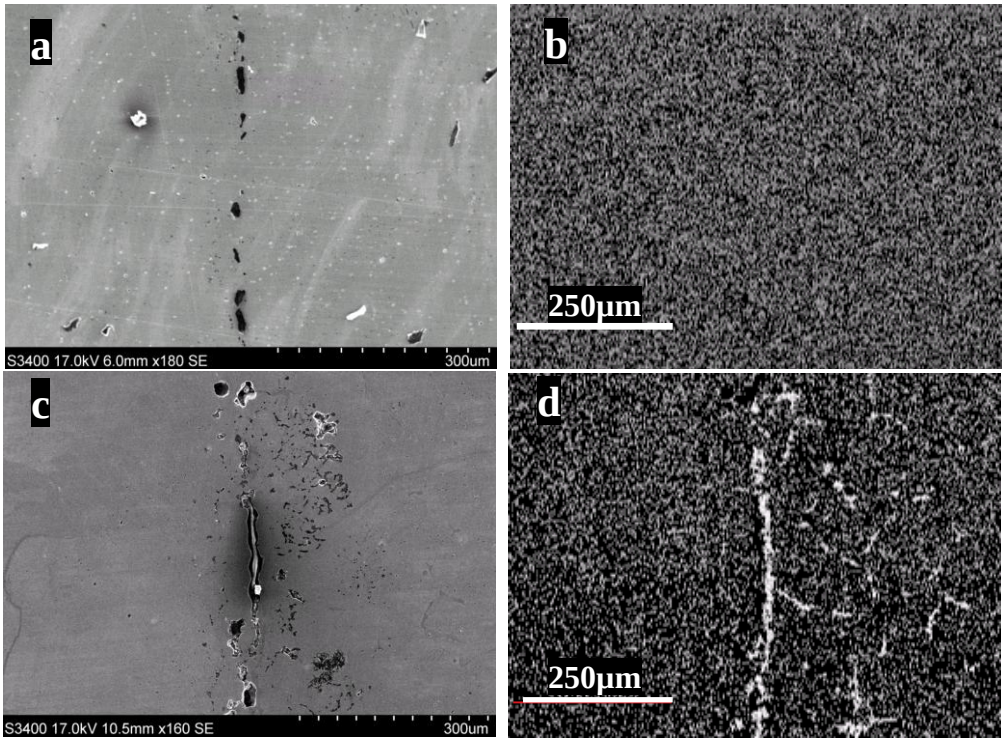

Figure 4.2: a) SEM micrograph of original cast iron/steel bar interface of 6a **b)** Element map of P at original cast iron/bar interface of 6a **c)** SEM micrograph of original cast iron/steel bar interface of 3a **d)** Element map of P at original cast iron/bar interface of 3a

The collector bar was made of hypoeutectoid steel that initially contained less than 0.06%C. Such steel should possess both pearlitic and ferritic microstructure as this composition lies halfway on the hypoeutectoid side of the eutectoid reaction line. However the detailed microstructural characterization given in Figure 4.3 (taken from the sample 6d) shows a fully pearlitic structure with proeutectoid cementite at the grain boundaries as the distance increases from the bar/cast iron interface (grain boundary phase is not continuous with the pearlite, this indicates that it's proeutectoid cementite not ferrite). To attain such a structure, a substantial carbon diffusion from cast iron into bar must have taken place during operation because pearlite with cementite at the grain boundaries indicates a hypereutectoid composition which is higher than 0.83wt%C according to the equilibrium Fe-C phase diagram, which corresponds to about 14 fold increment (0.77%) in the carbon content of the bar (Note that this discussion is based on the case where the effect of magnetic fields is omitted from the equation. Magnetic effect will be discussed in the next). The conclusion that steel bar is fluxed with carbon diffusion from the cast iron as explained above also implies that carbon

content of cast iron is replenished by carbon diffusion from the carbon block; because the cast iron that contains temper graphite means carbon content being maintained around the eutectic composition. If the cast iron layer was not provided with carbon from the carbon block, it would not have possessed large temper graphite but a microstructure representing hypereutectoid structure as it loses its carbon content to the steel bar; because 0.77% increase in the carbon content of the bar should have created a greater decrease in the carbon content of the cast iron as the volume of the bar is much greater than that of cast iron. Concomitantly, this decrease should have sufficed to bring the composition of cast iron to immediate vicinity of or within the hypereutectoid composition range (0.83-2%C) which would give partly pearlitic structure (or ferritic depending upon the alloying elements such as Si that promotes ferrite (41) and the cooling rate). Basing on the above discussion what can be stated is that there is a flux of carbon from the carbon block to the cast iron and steel bar and the bar tends eventually to attain hypereutectoid composition which in turn renders the bar electrically less conductive than its initial state.

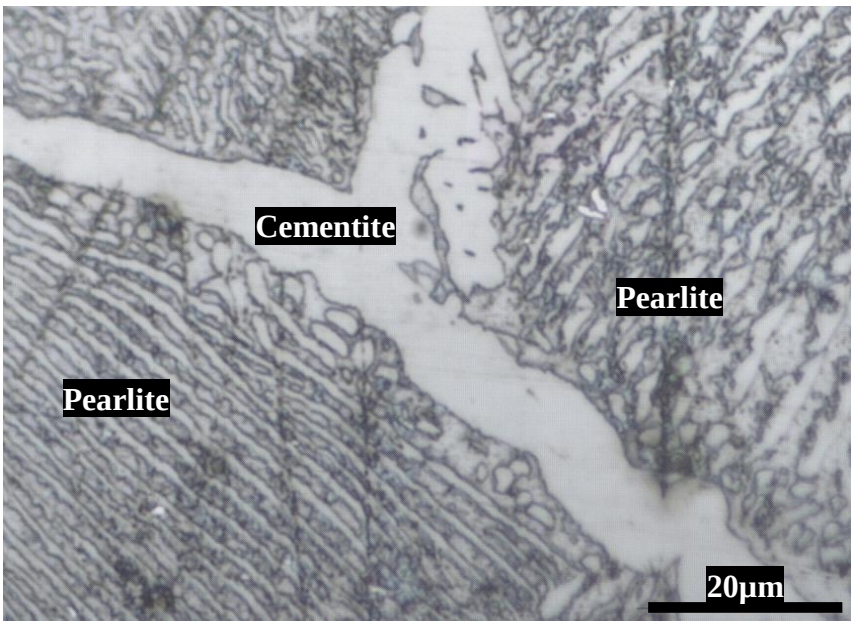

Figure 4.3: Pearlite colonies separated by proeutectoid cementite at the grain boundaries

Up until now we have disregarded the EDX results of 6a given in Table 3.1. We based our arguments on the microstructure as it is a product of heat treatment and composition. Particularly for steels and cast irons the final microstructure is an important tool to estimate the composition. Table 3.1 presents an anomaly in carbon concentration that is not compatible

with the observed microstructures. In the case of 6a, carbon concentration lies at 6.86wt%C near the carbon block/cast iron interface which is a value almost equal to the pure cementite composition, 6.67wt%C. In a similar fashion, a carbon content as high as 3.42wt% and 4.65wt% in ferrite and pearlite respectively was encountered at the interior of 6a. These compositions are in contradiction with those reported by Labrocque *et.al.*(32). They reported that carbon concentration of the cast iron decreased after operation. Considering the equilibrium cooling conditions the samples were subjected to, the observed microstructures seen in Figure 3.2-a somewhat deviate from those that must have been dictated by Fe-C equilibrium diagram (see Appendix-B, Figure B-1). The microstructure in Figure 3.2-b seems reasonable, because the coarse temper graphite reflects a high carbon content.

The anomaly associated with the ferritic and pearlitic regions with a C content of 3.42wt% and 4.65wt% respectively is that within these composition ranges and under equilibrium cooling conditions, the microstructure should have been identical to that found in Figure 3.2-b with the only difference being the size of the graphite particles; because as we enunciated earlier, the solidified cast iron after casting was cooled in such a condition that would promote the white cast iron which consists of cementite and pearlite. Thereafter, since the operating temperature of the cells are about 960^0C which maintains the bar at a temperature about 900-950^0C, the cementite must have been decomposed to austenite and spheroidal graphite. Upon cooling down to room temperature under equilibrium conditions, austenite must have decomposed into ferrite and graphite as well. The graphite formed by the decomposition of the austenite must have precipitated onto the spheroidal graphite that was already present which was formed upon the decomposition of cementite. Basing on this argument, the observed ferritic and pearlitic structure can not be explained by the heat treatment and subsequent cooling. It is obvious that classical approach that employs the equilibrium Fe-C phase diagram is not sufficient to interpret the existence of the observed microstructures in 6a. Therefore we should search for another explanation that circumvents the equilibrium phase transformations and involves significant shifts in the equilibrium Fe-C phase diagram.

The main thrust for our showing great interest in the microstructures is the fact that each microstructure exhibits different electrical properties which may alter the CVD in cathode assembly. However as the operating temperature (950^0C) corresponds to an austenitic matrix, we are only interested in the effects of the solutes elements in austenite and the morphology of the graphite particles in the austenitic matrix (see Appendix A6-A7). Bohnenkamp *et.*al (42)

reported that the carbon, after the nitrogen, has the highest elemental resistivity in austenite while the effect of aluminum and manganese was found to be insignificant (see Appendix A8 for the chemical analysis of the steel in the sample 6d). Graphite is known to be the less electrically conductive microconstituent of cast irons (43). Especially, in the case of interconnected flake graphites, conductivity of cast irons is reduced dramatically, whereas disconnected nodular graphites provide conductivity close to that of steels (43). Hence maintaining nodular or malleable graphite in austenitic matrix is beneficial for the electrical conductivity.

4.2. Effect of the magnetic field on the equilibrium Fe-C diagram

Nowadays, a technique that controls the microstructure of materials using the magnetic field has been attracting the researcher's attention (42-48). As this technique is only compatible with the materials in solid state and ferrous alloys undergo many solid/solid phase transformation, almost all of the projects were dedicated to the microstructure control of the cast irons/steels by the application of the magnetic field. The probability of such an effect in the aluminum reduction cells, albeit speculative because the average magnetic field induced by the current in the cell is about 0,01T (51), can not be excluded from discussion. However we calculated the magnetic field within the collector bar for a cell of 350 kilo-ampere and reached a value as high as 1T. Equation 4.1 gives the ampere's law we used;

$$B = \frac{\mu_0 . I}{2\pi r} \qquad [4.1]$$

where B represents magnetic field (Tesla), μ_0 is the permeability constant ($4\pi.10^{-7}$ weber.ampere^{-1}.meter^{-1}), I is the current (Ampere) and r is the radius of the conductor (meter).We assumed the collector bar to be cylindrical with a radius of 0.07 m.

Since the magnetic field is associated with the additional energy that is capable of imposing a shift in equilibrium diagram, thermodynamic evaluation of this energy is crucial for elucidating the mechanism involved. At constant pressure, under the magnetic field, Gibbs free energy change of a system can be given by;

$$dG = -SdT - MdH \quad [4.2]$$

where G, S, T, M and H represents, Gibbs free energy, entropy, temperature[4], magnetization and applied magnetic field strength, respectively.

Similarly, the chemical potential of an element, 'i', under magnetic field is given by;

$$\mu_i = G_i^0 + RTlna_i - M_i dH \quad [4.3]$$

The chemical potentials of Fe and C in both α and γ phase at equilibrium are given by;

$$\mu_{Fe}^{\alpha} = \mu_{Fe}^{\gamma} \qquad and \quad \mu_C^{\alpha} = \mu_C^{\gamma} \quad [4.4]$$

Combination of the equations 2 and 3 gives;

$$\Delta^0 G_{Fe}^{\alpha \Rightarrow \gamma} = RT\left(lna_{Fe}^{\alpha} - lna_{Fe}^{\gamma}\right) + \int_0^H (M_{Fe}^{\gamma} - M_{Fe}^{\alpha})dH \quad [4.5]$$

and

$$\Delta^0 G_C^{\alpha \Rightarrow \gamma} = RT\left(lna_C^{\alpha} - lna_C^{\gamma}\right) + \int_0^H (M_C^{\gamma} - M_C^{\alpha})dH \quad [4.6]$$

Based on the Equations 4.5 and 4.6, neglecting the magnetic free energy of the carbon, Choi *et.al* (44) calculated the Fe-C binary phase diagram under varying magnetic field effect. Figure 4.4 depicts the effect of magnetic field on the Fe-C equilibrium diagram.

[4] It should be noted that above the curie temperature, paramagnetic susceptibility data is used to calculate the magnetic contribution

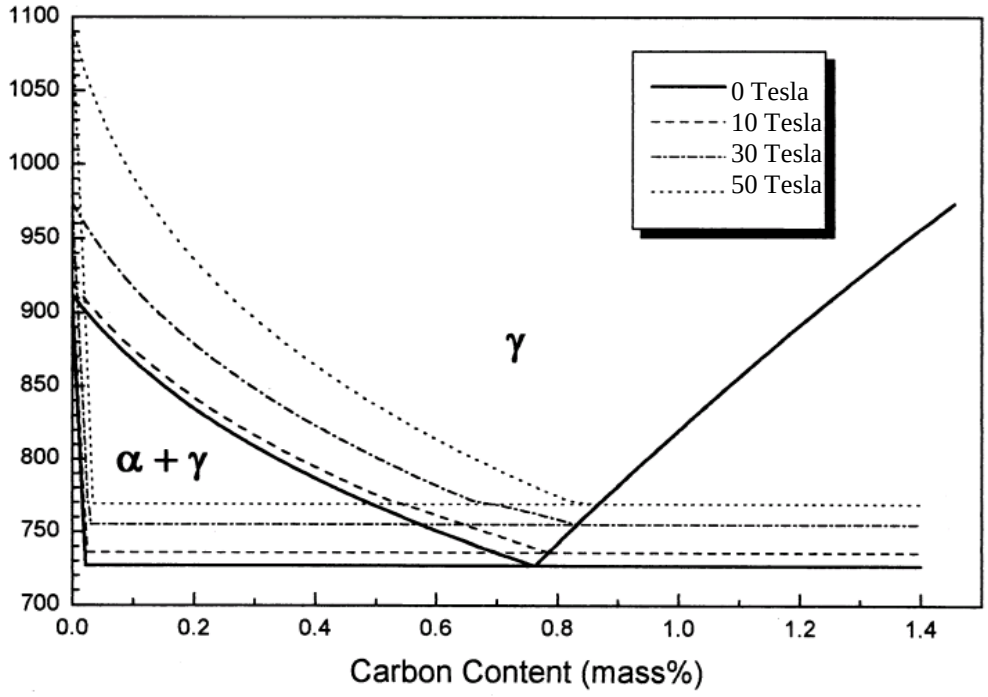

Figure 4.4: Effect of the magnetic field on equilibrium Fe-C phase diagram (44)

As evident from the diagram, the linear relation between the extent of the shift and the magnetic flux density can be drawn, that is, the higher the magnetic field applied, the more impact will be on the equilibrium diagram. It also can be deduced (44) from the diagram that under the magnetic field;

- Both the carbon content of eutectoid composition and the eutectoid temperature increase
- $\alpha \Rightarrow \gamma$ transformation temperature increases (Increased ferrite stability)
- Carbon solubility in ferrite increases

The reason ferrite is stabilized over austenite under magnetic field is due to the fact that magnetic susceptibility of ferrite is higher than that of austenite (44). They also figured that the extent of changes in the microstructure (in their case the ferrite content increased more than what was predicted by the thermodynamic approach) could not have been achieved by the Gibbs energy change alone. Therefore, they referred to the effect of the magnetic field on the phase transformation kinetics (i.e., intervened diffusion of carbon in austenite, change in nucleation and grain growth kinetic). These are very important findings for shedding the light on the fully ferritic and pearlitic structures observed with our sample. It was given earlier in Table 3.1 that in spite of the significantly high carbon content given in Table 3.1, neither

pearlite formation nor graphite precipitation was observed in the ferrite and pearlite regions which possibly can be attributed to the increased carbon solubility in ferrite. However this must be taken as only a contributing factor, because as we calculated earlier in Equation 4.1, the magnetic field generated by the current passing the collector bar cannot provide the sufficient energy to make the observed changes. From this argument and the plot above what can be claimed with intuitive certainty is that induced magnetic field causes both an enhanced solubility of carbon in ferrite and alteration of the kinetic factors and that it is likely that these phenomena are among the contributing factor to the observed anomalies within sample 6a given in Figure 3.2.

Another point we would like to draw the attention is that the change in $\alpha \Rightarrow \gamma$ transformation temperature. This might provide a gain in electrical conductivity as the ferrite is more conductive than the austenite (At 313K, the pure austenite has a resistivity of 0.34 μΩm (42) while ferrite has 0.1 μΩm (43) at 300K). If we manage to bring this alteration in the transformation temperature by controlling the magnetic field so that the ferrite is maintained at the operating temperature, this would be a profit with regard to the electrical conductivity.

4.3. Al and Na in Cast Iron and the Collector Bar

Among the several notable features in elemental map in Figure 3.3 discussed earlier, the most intriguing one appears to be the presence of aluminum and sodium in cast iron, particularly their accumulation on temper graphite in cast iron, because these elements are not among the constituents of cast iron and steel bar. Labrecque *et.al.*(32) reported an Al content of 6.8wt% while our quantification shows 14.40wt%Al (Table 3.1). Their analysis is in consistency with our analysis for the ferritic region seen in Figure 3.2-a. In addition to the difference in aluminum concentration, they did not detect any sodium in the rodding. From this two comparisons what seems reasonable to claim is that they did not observe accumulation of aluminum and sodium in the temper graphite particles, because the majority of sodium and aluminum we detected are within the temper graphite.

The presence of aluminum and sodium far from the cathode surface indicates either metallic infiltration through the cracks in the carbon block or the bath penetration with subsequent liquid aluminum forming reaction as given in the Equation 1.9. It is a well known phenomenon that aluminum can penetrate down to the cast iron and form Al-Fe alloy that

contributes to cathodic voltage drop (21) . What needs further discussion is why Al and Na accumulate on the temper graphite in cast iron while the graphite is deprived of the other major alloying elements.

As shown in Table 3.1, EDX system did not detect any Na within the region encompassing ferrite and pearlite where almost no graphite is present in Figure 3.2. This may be taken affirmative for Na being associated with the presence of temper graphite in cast iron (if not to be correlated with other variable). There are two possible suggestions that might tentatively be put forward to explain this phenomenon:

- Na, as suspected by Stagg (29), favors the carbon transfer from the carbon block to the cast iron, or
- Na(g) transportation is facilitated through the pores of graphite in the cast iron.

The fact that the standard Gibbs energy of the Equation 1.9 in the given direction is negative which ensures the stability of NaF over the sodium in carbon and that the element mappings for sodium and fluorine do not occur at the same pixel regions explicitly mean that although NaF is thermodynamically favored at operating temperature, the sodium accumulated on temper graphite in cast iron does not necessarily represent the NaF yielded by above reaction. At this stage, suggestion 'b' seems to be more plausible explanation. At the operating temperature of 950^0C, sodium evaporates and it is likely to be adsorbed in the graphite pores in cast iron structure. It should also be mentioned that the element map of fluorine is dominantly influenced by the energy emitted from iron and it is present only as a trace element (Fluorine content is difficult to measure). Additionally, in order to make the element maps clearer, contrast was deliberately increased. Hence it may be assumed that the sodium map consists of mainly background noise except the region where sodium overlaps the carbon in the map. It should also be noted that sodium has a negligible solubility in iron (see Appendix-A9), which is also evident from the Table 3.1, therefore the transport in vapor state is more reasonable explanation for sodium being in the cast iron. Figure 4.5 shows half graphite particles in the cast iron (highlighted with orange marker). One can assume that the other half was embedded in the carbon block. Therefore we may these graphites are used by the bath components as the gateway into the cast iron.

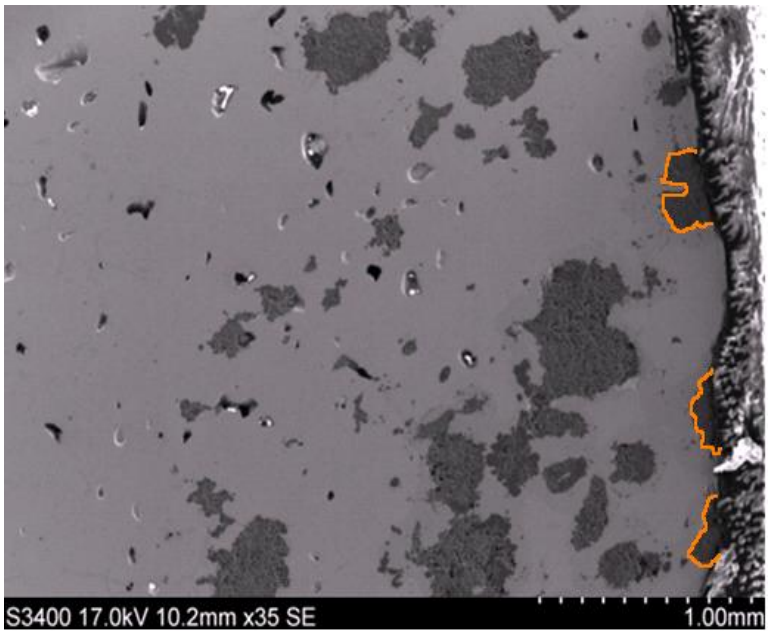

Figure 4.5: SEM micrograph of 6a with a marker highlighting the graphite particles at block/cast iron interface

The same mechanism may also embrace the Al accumulation on temper graphite. However this should be taken only as a contributing factor to overall Al concentration in the cast iron. Aluminum can dissolve in iron more than sodium and readily react with iron to form various intermetallics (see Appendix-A10). Additionally, we may speculate that its higher concentration in porous structure of graphite compared to the matrix and the depletion of iron in temper graphite also indicate that aluminum exist in liquid metal form filling the pores. Because if it entered in graphite as Fe-Al alloy, we would have observed Fe accumulation on graphite as well, indeed Figure 3.3 explicitly displays iron deficiency in graphite. As we already know from the Equation 1.9, aluminum is in liquid state at the operating temperature and if it does not form an alloy with iron, its presence on temper graphite can only be explained by its infiltration into the pores. Therefore, we may state that not only does aluminum enter the cast iron through Fe-Al alloy formation at carbon block/cast iron interface but also it fills the pores of graphite as liquid metal and enters the cast iron in a similar manner as Na vapor does.

Another argument supporting the above discussion, although it may sound speculative, is that temper graphite is enriched with only the bath components (Na, Al, Ca) not with the alloying elements of cast iron. This might be taken as affirmative that these elements exploit the temper graphite as a gateway into the cast iron (This statement will be challenged in the

upcoming discussions). The initial carbon content of cast iron, 2.8-3.2 wt%, must have resulted in white cast iron structure consisting of cementite plus pearlite, otherwise there would not have been temper graphite in the ferritic matrix, because the white cast iron is the precursor to the development of such microstructures. As the sealing process is performed by resistance heating which also generates magnetic field stronger than the line current, the carbon solubility in iron is already enhanced before the cells start to pass current. Therefore the driving force for temper graphite precipitation from cementite should have been less than what is predicted by the equilibrium diagram. Hence, when the temperature reached 900-950^{0}C as the cell started to pass current, instead of complete transformation into temper graphite, a portion of the carbon rejected by the cementite should have dissolved into austenite (austenite is formed upon decomposition of cementite at 900-950^{0}C). Therefore, the transformation into temper carbon should have continued as the carbon diffusion from the carbon block -which supposedly already contains the elements of the bath- proceeded (It should be stressed that the carbon block is soaked with the bath components within hours after start-up. This is in consistency with the proposed mechanism as it suggests an extended time for temper graphite formation. As also can be seen in Figure 3.4 and Figure 3.7, temper graphite formation process has not been completed yet within the sample S1.

4.4. Temper Graphite Formation and the Kinetics

Figure 3.4 and 3.7 show flake graphite and pearlitic matrix indicating that the cast iron solidified into grey cast iron. However it is also seen that temper graphite embedded in a fully pearlitic matrix formed close to the sidewall as well which points the rapid cooling rates in the vicinity of the sidewall. One interesting feature in Figure 3.7 and 3.9 is the agglomerated graphite flakes forming spheres and encapsulating the matrix and eventually attaining a shape that resembles that of temper graphite. To the author's knowledge, there is no such a phenomenon published in the literature. The morphology of the graphite that formed upon solidification after casting can not be modified by heat treating the cast iron (52). Therefore, the temper graphite can only form upon heating the cementite up to malleabilization temperature (~900-950^{0}C) and flake graphite cannot turn into temper graphite unless it dissolves first. Thus the temper graphite formation through encapsulation of the matrix seen in Figure 3.7 and Figure 3.9 is an entirely new mechanism. This new mechanism may be explained by the alteration of the phase transformation kinetics as mentioned earlier.

As pointed in Figure 3.7 and supported by the element map given in Figure 3.8, what we defined as temper graphite indeed majorly consists of Al-Na-F elements which is similar to what we postulated earlier in Figure 3.3 for the sample 6a with a minor difference being the element map of fluorine. Graphite is present as flake graphite in this temper-graphite-like structure. Figure 3.7 and Figure 3.9 help us challenge our initial statement and adopt a different approach to explaining the presence of aluminum and sodium in the temper-graphite-like particles which endorses us to ask the question 'if it is possible that the flake graphite colonies form a sphere encapsulating the matrix out of which the constituents of the cast iron except aluminum and sodium are driven resulting in a final composition given in Table 3.2 and shown in Figure 3.2-b. Figure 3.9 was taken from the inside of the white circle shown in Figure 3.4. A foundry man would confidently define it as temper graphite due to its irregular nodular shape, however the graphite flakes associated with its surroundings suggest that it was formed by such a mechanism as explained above (encapsulation hypothesis). On the contrary to what we enunciated earlier that 'not the entire particle consists of graphite, but only a small portion does while the rest is the Al-Na-F rich phase', the temper graphite in Figure 3.9 consists dominantly of graphite. Neither aluminum nor sodium accumulation is seen. This may mean that aluminum and sodium diffusion into the cast iron (not the graphite) did not progress at a sufficient rate. If it was then we would have seen their accumulation in the graphite as well. Such behavior of aluminum can be explained by the limited diffusion of aluminum the iron. Karfoul *et.*al. (53) reported that during a diffusion bonding process of carbon steel to aluminum, at temperatures below the melting point of aluminum, aluminum diffusion into the steel was not detectable. Therefore we may suggest that the reason we did not observe aluminum accumulation in the temper graphite seen in Figure 3.9 is that aluminum diffusion into the cast iron was not sufficient after one week in operation to appear to be the dominant element of the phase in which it is present. This statement is confirmed by the chemical analysis of the surrounding (see Appendix-A2 for the chemical analysis of the surrounding matrix). One other explanation to this slow diffusion process could be the retarded diffusion process by the magnetic field. Nagamichi *et.al.* (50) reported that carbon diffusion in austenite was enhanced under a negative magnetic field while it was retarded when a positive field was applied. To the author's knowledge there has not been any report on the effect of magnetic field on the diffusion of aluminum or sodium in iron. Thus we may tentatively claim that the matrix encapsulated by the graphite flakes did not contain adequate aluminum and element mapping therefore did not identify an aluminum accumulation (This is

a contradictory hypothesis to the one we claimed earlier for the presence of aluminum and sodium in the cast iron).

Figure 4.6 shows that the head of aluminum and sodium in temper graphite is 620µm away from the sidewall, while it is approximately 2.5mm in the case of the sample 6a (Figure 3.3). It is an indication that aluminum and sodium in graphite reach deeper into the cast iron as the time passes (pointing diffusion). However whether the time dependent variable is carbon diffusion associated with aluminum and sodium (or NaF) transport or their individual diffusion in the cast iron remains unclear.

In the element mapping in Figure 3.9-b, it is seen that neither of these elements are accumulated in graphite. Based on this observation we may further claim that sodium, fluorine and aluminum behaves similarly, that is, when aluminum is in the graphite so are sodium and fluorine as seen in Figure 3.8. On the contrary to the situation seen in Figure 3.3 where fluorine is depleted in the graphite, Figure 3.8 indicates that fluorine indeed is present in the graphite overlapping aluminum and sodium in the early stages of the cell operation. Relying on this and referring to the Equation 1.9, we may predict that $Al_{(l)}$ and $NaF_{(l)}$ are the stable products and at least during the first week of the operation (S1 was taken from the cell after one week in operation) they remain as such. Their being in liquid state during operation is a detrimental factor for electrical conductivity. However in order to estimate how long until NaF decomposes and the fluorine leaves the graphite should be studied with samples taken from the cells shut down at different operation times.

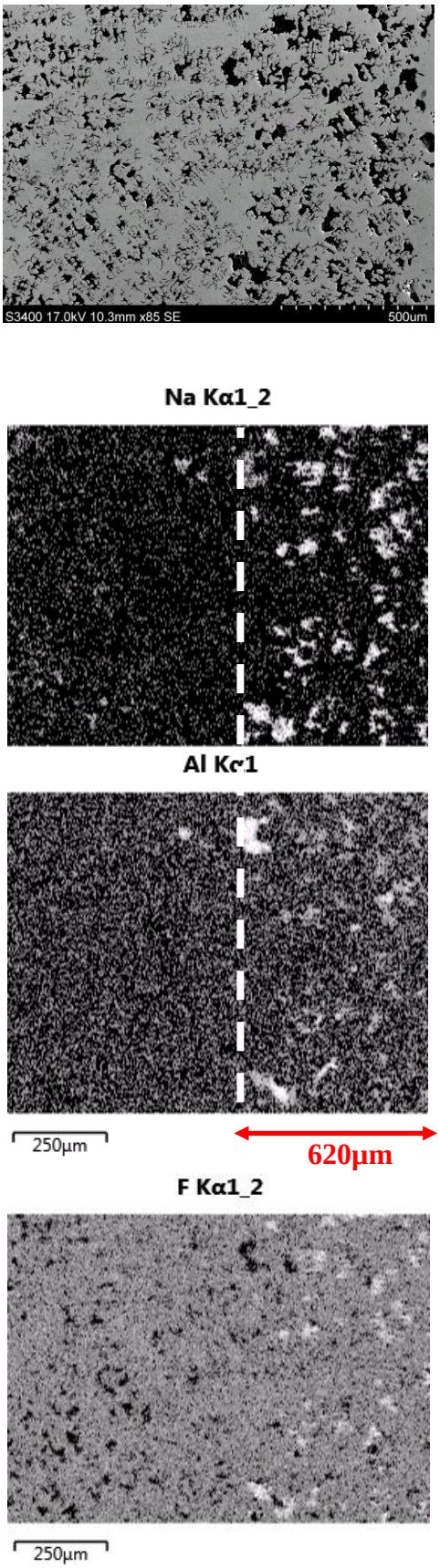

Figure 4.6:a) SEM micrograph of section 3a and corresponding element maps of **b)** Al **c)** Na and **d)** F

4.5. Aluminum Oxide in Temper Graphite

In addition to the enrichment of the graphite with metal constituents, oxygen accumulation on temper graphite as seen in Figure 3.3 is a noteworthy feature and deserves a discussion because if it corresponds to Al_2O_3, this may cause a sharp damage in electrical conductivity in cast iron. Such a phase was previously reported by Xue at bar/ramming paste[5] and ramming paste/carbon block interface (4). He reported the presence of a 'white layer' which he named alumina after EDX analysis (The sealing material was ramming paste instead of cast iron at that time).

The chemical analysis tabulated in Table 3.2 can be used to calculate the ratio of stoichiometric coefficient (m) of O to Al as following;

$$\frac{m_O}{m_{Al}} = \frac{35.20/16}{33.41/27} = 1.78 \tag{4.6}$$

which approximately corresponds to the stoichiometric ratio of O to Aluminum, 1.50, in Al_2O_3. Therefore, aluminum and oxygen accumulated on the temper graphite reasonably likely to exist as Al_2O_3 which is detrimental for the electrical conductivity.

4.6. Cracks along the Cast Iron/Carbon Block Interface

An increased magnification SEM image revealed another significant finding that is quite likely to be another contributing factor to the increased CVD. Figures 3.10-a and the corresponding element map, Figure 3.10-b, were taken from the outermost layer of the cast iron in 6a where it was in direct contact with the carbon block during operation. It is clearly seen on the image that a crack exists along the cast iron in the vicinity of cast iron/carbon interface. This crack was detected to intermittently exist (see Appendix-A3 for more pictures). One major challenge we had at first sight was that it was not certain if the part darker part was cast iron or the debris from the carbon block. Although the contrast difference between the two sides and the element mapping for oxygen (since the carbon block is porous in nature, it

[5] Ramming paste is a carbon based plastic once used to seal the sidelining and collector bars

contains air) suggest that it is the debris, the element map of Si questions the validity of this suggestion as it is found at a higher concentration within the lighter part than that within the darker which simply indicates that the phase within the darker part is cast iron.

The crack initiation is likely to have occurred during the operation otherwise we would not have observed a leap in concentration of some elements from one side to the other. In the case of Si, an alloying element for cast iron, it is expected to diffuse from cast iron to the interior of the steel due to the concentration gradient (see Table 2.1). However, the Si content of the darker side was precluded from diffusion into the lighter side by the gap while the Si content of the lighter side had no obstacle to diffusion, which resulted in higher Si concentration in the darker side. On the other hand, element mappings for Aluminum and Mn challenge this suggestion. Their distribution on either side exhibits a contrary behavior to that of Si. The nature of their behavior remains unclear.

One possible reason for crack initiation is the expansion/contraction behavior seen in cast iron upon solidification and heat treatment. High casting temperature or improper cooling rate could result in crack initiation. Another possibility is the increased volume by the intake of bath materials and carbon into the cast iron. However mechanical consideration is not within the scope of this thesis.

4.7. Debris From the Top Cast Iron

The optical micrograph and the element map of the top layer of 4d presented in Figure 3.11 and Figure 3.12 respectively, feature a phosphorous rich phase preferentially positioned on top and at the grain boundaries of the columnar ferrite. Its yellowish appearance resembles the iron phosphide eutectic seen in most cast irons either as binary (Ferrite-Fe_3P) or ternary (Ferrite/Fe_3P/Cementite) depending on whether the cast iron is grey or white respectively. It is probably the ternary phosphide eutectic that consists of ferrite/phosphide/cementite because as we declared earlier the cast iron had solidified into white cast iron and the ternary eutectic melts at ~950^0C compared to binary eutectic with a melting point of 1050^0C (54, 55) (see Appendix-A11 for the binary and ternary phase diagrams). The accumulation of phosphorous rich phase on top indicates that there might have been a crack in the cast iron during solidification after casting and that the liquid phase filled the crack cavity. An illustration describing this is given in Figure 4.7.

By performing a simple calculation using the data tabulated in Table 3.3, we may conclude that the top layer lying on the columnar ferrite grains consists primarily of Fe_3P (The stoichiometric coefficient of Fe to P in Fe_3P is '3'. This phase was found by Kurosawa et.*al.*(56) to be the last phase to solidify at a temperature below its melting point. They stated, upon cooling it remains as a liquid film down to 900^0C.

$$\frac{m_{Fe}}{m_P} = \frac{{}^{78.46}/_{55.84}}{{}^{12.93}/_{30.97}} = 3.36 \qquad 4.7$$

In order to prove aforementioned mechanism we examined the chemical composition of the debris. If this mechanism takes place, the debris then would not contain any P as it looses its P content to the cavity (we assume an accelerated diffusion in liquid state and penetration into the cracks). The SEM and optical micrographs and the element map of the debris are given in Figure 3.14-a, Figure 3.14-b and Figure 3.15 respectively. As identified by EDX analysis (Table 3.4), the debris doesn't contain[6] phosphorous confirming the above hypothesis.

Another point that should be emphasized is the high aluminum content in the debris. It is seen that aluminum is the predominant element and evenly distributed throughout the whole sample. Its footprint overlaps that of iron indicating an iron loss from cast iron due to alloying and subsequent backflow of the alloy up to the metal pad as described by Sørlie et al. (21).

It should be mentioned that we did not detect any such layer enriched with P on top of the other row "1" member samples. In the case of S1, this is simply because there might have not been a crack initiation during operation. However in the case of S2, we need another explanation because we already assumed that it possesses a crack on top of it. The most conceivable approach could be that as the cell starts cooling down, sides of the bar is the first to cool and the liquid phosphide accumulates on the bar center (equal distance from the both sides) where the sample 4d was extracted and when the temperature is below its melting point it solidifies in the center.

[6] Quantification was performed multiple times. Some analysis detected 0.001-0.002wt.%P, while the majority did not contain any P.

Figure 3.14 and Figure 3.15 implicitly confirms our first suggestion that NaF is present in cast iron in liquid state. It is seen in Figure 3.14 that the shape of NaF resembles that of phosphide eutectic (concave triangular). This actually indicates that after phosphide eutectic melted and left the debris forming a layer inside the crack, the empty grain boundaries in the debris that were occupied by the phosphide eutectic is now filled by the liquid NaF. This is why its shape is exactly the same as the phosphide eutectic.

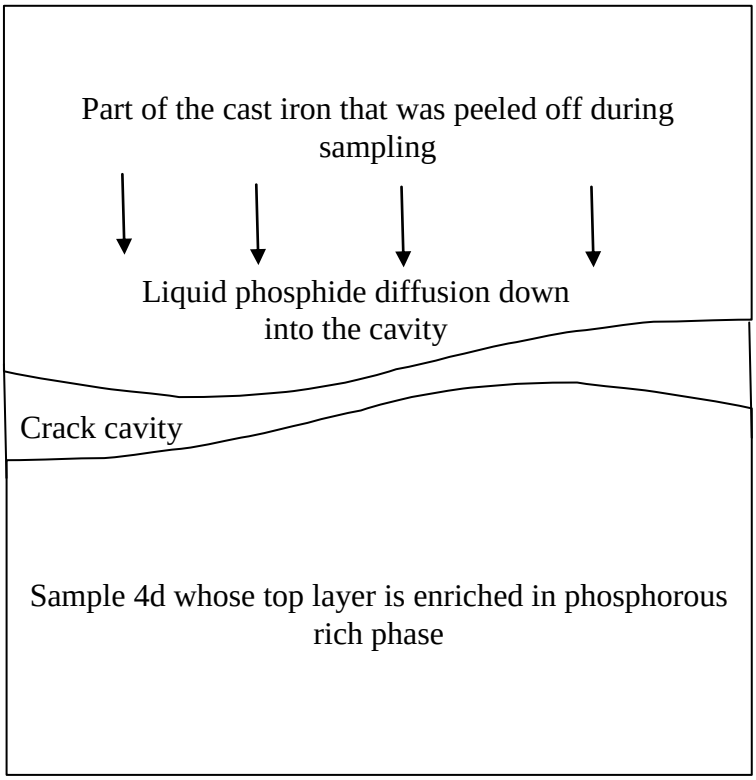

Figure 4.7: Description the phosphorous rich layer formation on top of the cast iron layer in 4d

5. CONCLUSIONS

As the ravenous demand for aluminum products and the associated power costs are expected to continue rising, the industrial leaders will be compelled to take unprecedented measures to reduce the production costs. Among the measures such as improved current efficiency, electrolyte chemistry and electrode engineering, the cathodic voltage drop at carbon/cast iron/collector bar interface must be handled adopting a radical approach with modified cast iron chemistry. There is no doubt that the fields of metallurgy and physical chemistry are both required to understand and interpret the nature of the physical and chemical changes occurring in and the surroundings of the collector bar and their effect on the CVD and the cell parameters.

Based on the findings presented in this thesis, following conclusions can be drawn;

1 The present work highlights the deleterious effects of the high phosphorous cast iron. Ternary phosphide eutectic (liquid at the operating temperatures) forming a network at the cast iron grain boundaries was detected. On the side of the 6-years-old sample, the network was not detected, while on the side of 7-days-old sample the network reaching the cast iron/steel bar was encountered. On top of the collector bar, it was found that a thick layer of Fe_3P on top of the bar formed probably due to the cracks in the cast iron.

2 The cast iron layer was found to be the vital part of the bar/cast iron assembly. The temper graphite in the cast iron is suspected (more experiment is necessary to confirm) to serve as the gateway for the elements coming from the bath to enter the cast iron. As a consequence Na, Al, F followed by Ca were found to be present in the cast iron, while Al was detected even further into the steel bar. Aluminum and NaF was

suspected to exist in their liquid form in temper graphite within the 7-days-old sample at operating temperatures, while Al_2O_3 was found in the temper graphite within 6-years-old sample.

3 It was found that the cast iron was solidified into a mixture of grey and white cast iron. One should aim to obtain white cast iron as it is precursor to the malleable cast iron which is more conductive than grey cast iron.

4 It was shown that carbon content of the cast iron and the steel bar does not reflect their microstructures. Their possession of higher carbon content than what is imposed by the equilibrium Fe-C diagram was found to be attributable to the effect of the magnetic field. It was shown that magnetic field is capable of bringing a shift in the equilibrium Fe-C diagram.

5 A new mechanism for temper graphite formation was described and attributed to the alteration of the nucleation kinetic by the magnetic field. This alteration is also suspected to contribute to the observed microstructures that don't reflect the equilibrium Fe-C diagram. It was also pointed out that the magnetic field might change the diffusion rate of carbon in iron either negatively or positively depending on the magnetic field gradient (if any).

6 A crack along the cast iron/carbon interface was detected. This was evaluated as a contributing factor to the cathodic voltage drop.

It should be mentioned that the measurement of the single effect of the suggested changes is challenging. A statistical evaluation of many cells will probably be needed.

SUGGESTIONS to FURTHER WORK

The very fact that phosphorous eutectic is in liquid form at operating temperatures is a serious treat for the cathodic voltage drop with regards to both contact pressure and its low electrical conductivity. Therefore, the cast iron grades with lower phosphorous content would be of beneficial for improved energy efficiency.

The temper graphite formation and associated aluminum and sodium transport should be investigated in detail. One suggestion could be to carry out an experiment where a cast iron specimen is heat treated in a Na vapor atmosphere to monitor the Na transport into the cast iron. Another experiment may be carried out where a cast iron specimen is exposed to the liquid electrolyte. By doing so we may come to an adequate understanding of the behavior of the bath elements in the cast iron and utilize this in minimizing the amount of these elements in the cast iron.

The effect of magnetic field both on the thermodynamics and the kinetics of the system must be studied in detail. To what extent this effect is important should be clarified as well.

There is no doubt that the fields of metallurgy and physical chemistry are both required to understand the nature of the physical and chemical changes occurring in and the surroundings of the collector bar and their effect on the CVD and the cell parameters.

REFERENCES

(1) Grjotheim, K., Kvande, H., *Introduction to Aluminium Electrolysis,* Aluminium-Verlag, ISBN 3-87017-233-9, Düsseldorf, p.1,1993.

(2) Lorentsen, Odd A., '*Behaviour of Nickel, Iron and Copper by Application of Inert Anodes in Aluminium Production',* (Ph.D. thesis), NTH, Trondheim, ISBN 82-7984-133-4, no.104, p.1, 2000.

(3) Kvande, H. and Haupin, W., *Inert Anodes for Al Smelters: Energy Balances and Environmental Impact,* JOM 53. (5), 2001, pp. 29-33.

(4) Xue., J., *'Inspection of Cathode Collector Bars From Aluminium Reduction Cells',* Sintef Applied Chemistry Inorganic Process Chemistry and Analysis, Project Report no.STF66F99067

(5) Dupuis, M., Tabsh, I., *Modeling Of Aluminum Reduction Cells Using Finite Element Analysis Techniques,* Light Metals 1995, TMS, pp. 295-299.

(6) Bockris, J., Reddy, A.K., *Modern Electrochemistry 1;Ionics,* Plenum Press, ISBN 0-306-45554-2, New York, 2nd Edition, 1998, p.534.

(7) Hamann, C.H., Hamnett, A., Vielstich, W., *Electrochemistry,* WILEY-VCH, ISBN 978-3-527 31069-2, Weinheim, 2nd edition, 2007, p.417.

(8) Thonstad, J., Galasiu, R. and Galasiu, I., *Non-Aqueous Electrolytes,*

(9) Thonstad, J., Galasiu, R. and Galasiu, I. , *Inert Anodes for Aluminium Electrolysis,* Aluminium-Verlag, ISBN 978-87017-286-2, 2007.

(10) Kryukovsky, Vasylii, A. Frolov, Anton V., Tkatcheva, Olga Yu. Redkin, Alexander A., Zaikov, Yurii P., Khokhlov, Vladimir A. and Apisarov, Alexey P., *Electrical Conductivity of Low Melting Cryolytes*, Light Metals 2006, TMS, pp.409-413, 2006

(11) Thonstad, J., Fellner, P., Haarberg, G.M., Hives, J. Kvande, H., Sterten, A., *Aluminium Electrolysis: Fundamentals of the Hall Hèroult Process,* Aluminium-Verlag, ISBN 3-87017-270-3, Düsseldorf, 2001

(12) Skybakmoen, E., Solheim, A. and Sterten, A., *Alumina Solubility in Molten Salt Systems of Interest for Aluminium Electrolysis and Related Phase Diagram Data,* Met. Mat. Trans. B., 28B, pp.81-86, 1997.

(13) Lu, H.M., Fang, K.M., Qiu, Z.X., *Low Temperature Aluminum Floating Electrolysis in Heavy Electrolyte Na_3AlF_6-AlF_3-$BaCl_2$-NaCl Bath System,* Acta Metallurgica Sinica, vol.13, no.4, 2000, pp.949-954.

(14) Zhang,, M., Kamavaram, V. and Ramana, G.R., *New Electrolytes for Aluminum Production: Ionic Liquids,* JOM 2003 (9), pp.54-57.

(15) Apisarov, A. *et.al, Physical-Chemical Properties of the Kf-NaF-AlF_3 Molten System With LowCryolite Ratio,* Light Metals 2009, TMS, pp. 401-403, 2009.

(16) Yang, J., Hryn, John N., Davis, Boyd R., Roy, A., Krumdick, Greg K., Pomykala, Joseph A.,*New Opportunities for Aluminium Electrolysis With Metal Anodes in a Low Temperature electrolyte System,* Light Metals 2004,TMS, pp. 321-326, 2004.

(17) Beck, T.D., *A Non Consumable Anode for Production of Aluminium With Low Temperature Fluıoride Melts,* Light Metals, TMS, 1995, pp. 355-360.

(18) Fischer, W.K., Keller, F., Perruchoud, R.C and Oderbolz, S., *Baking Parameters and the Resulting Anode Quality,* Light Metals 1993, TMS, pp.683-694, 1993.

(19) Sele, T., *Instabilities of the Metal Surface in Electrolytic Alumina Reduction Cells,* Metallurgical Transactions B, vol.8B, pp.613-618, 1977.

(20) Sun, H., Zikanov, O. and Finlayson, B.A., *Effect of Background Melt Flow and Interface Distortion on the Stability of Hall Hèroult Cells,* Magnetohydrodynamics, vol.41, no.3, pp.273-287, 2003.

(21) Sorlie, M. and Oye, H.A., *Cathodes in Aluminum Electrolysis,* Aluminium-Verlag, ISBN 978-3-87017-294-7, 3rd Edition, 2010.

(22) Liao, X., " *Wear And Enhanced Sodium Expansion Of Carbon Cathode Materials In Aluminum Electrolysis*", PhD Thesis, Norwegian University of Science and Technology, 1998.

(23) Shamsili, T., "*Bath Penetration and Chemical Reactions in Carbon Lining of Aluminum Electrolysis Cells"*, PhD thesis, Norwegian University of Science and Technology, 1996.

(24) Sørlie, M. and Øye, H.A., "*A Survey On Deterioration Of Carbon Linings In Aluminum Reduction Cells*", Professor Dr.techn.Harald A.Øye Publications 1962-2004, pp.985-992.

(25) Dorward, R.C., " *Reaction Between Aluminum And Graphite In The Presence Of Cryolite*", Metallurgical Transactions 1973, vol.4, pp-386-388., 1973.

(26) Gullbransen, H., Sterten, A. and Ødegard, R. Light Metals 1992, TMS, p.521, 1992

(27) Grjotheim, K. and Welch, B.J., *Aluminum Smelter Technology: A Pure and Applied Approach*, Aluminum Verlag, ISBN 13: 9783870171322, 1980, p.67.

(28) Krohn, C., Sørlie, M. and Øye, H., "*Penetration Of Sodium And Bath Constituents Into Cathode Carbon Materials Used In Industrial Cells*", Professor Dr.techn.Harald A.Øye Publications 1962-2004, pp.999-1012

(29) Stagg, J.A., '*Reduction Cell collector Bars-Interaction With Operating Environment and Influence on Cell Operation'*, Light Metals, TMS, 1981, pp.397-406

(30) Charnock, W., Taunt, R.J., '*Carburization of Crevices in Impure Sodium',* Metallurgical Transactions, vol. 9A, 1978, pp. 880-881.

(31) Haupin, W., *' Cathode Voltage Loss in Aluminum Smelting Cells'*, Light Metals, TMS, vol.1, pp. 339-349.

(32) Labrocque, Chantal., Gagnè, M., Lavoie, D., Lèvesque, A. and Murphy, B., *'A new Technology for Cathode Rodding Used in Aluminum Electrolytic Cells'*, Light Metals, TMS, 2003, pp. 661-667.

(33) Vander Voort, G., F., '*Applied Metallography*', Van Nostrand Reinhold Company, ISBN 0-442-28836-0, 1986, p.41.

(34)Orvis, K., H. and Grissino, H., D., *'Standardizing the Reporting of Abrasive Papers Used to Surface Tree-Ring Samples'*, Tree-Ring Research, vol.58 (1/2), 2002, pp.47-50.

(35) Vander Voort, G., F., '*Applied Metallography*', Van Nostrand Reinhold Company, ISBN 0-442-28836-0, 1986, p.1

(36) Goldstein., J.I., Roming Jr., A.D., Newbury, D.E., Lyman, C.E., Echlin, P., Charles, F., Joy, D.C., Lifshin, E., *Scanning Electron Microscopy and X-Ray Analysis*, Plenum Press, ISBN 0-306-44175-6, 1992.

(37) Ochal, P., *Carbon-supported Ru@Pt Core-shell Catalyst for Low Temperature Fuel Cells*, Doctoral Thesis, NTNU, 2012, ISBN 978-82-471-3329-3

(38) Cingi, C., Rauta, V., Niini, E. and Orkas, J., *"Cast Bonding of Cast Irons to Ferritic Stainless Steels"*, Materials Science Forum Vols.654-656, 2010, pp.2712-2715, 2010.

(39) Calvo, F.A., Urena, A., Gomez de Salazar, J.M., Molleda, F., *"Diffusion Bonding of Grey Cast Iron to ARMCO Iron and a Carbon Steel"*, Journal of Materials Science Letters, vol.24, pp.4152-4159, 1989.

(40) Majerová, V., Radomilla, K. and Gianni, N., 'Structural Analysis Of En – GJL 300 Castings By Metallographic Techniques', 4th Youth Symposium on Experimental Solid Mechanics = 4th YSESM : May, 4th-7th 2005 Castrocaro Terme (Italy) : session "C". - Bologna: University of Bologna, 2005, pp. 67-68, ISBN-88-901080-2-9

(41) Krause, D. E., "Grey Iron-A Unique Engineering Material" Grey, Ductile, and Malleable Iron Castings-Current Capabilities, ASTM STP 455, American Society for Testing and Materials, Philadelphia, 1969, pp. 3-28).

(42) Bohnenkamp, U. and Sandström, R., '*Electrical Resistivity of Steels and Face Centered Cubic Iron'*, Journal of Applied Physics, vol.92, no.8, 2002, pp. 4402-4407.

(43) Velichko, A., Wiegmann, A. and Mücklich, F., '*Estimation of the Effective Conductivities of Complex Cast Iron Microstructures Using FIB-Tomographic Analysis*, Acta Materialia, vol.57, 2009, pp. 5023-5035.

(44) Choi, J.K., Ohtsuka, H., Xu, Y. and Choo, W.Y., '*Effects of a Strong Magnetic Field on the Phase Stability of Plain Carbon Steels*', Scripta Materialia, vol.43, 2000, pp. 221-226.

(45) Ohtsuka, H., ' *Effects of a Strong Magnetic Field on Bainitic Transformation*', Current Opinion in Solid State and Materials Science, vol.8, 2004, pp. 279-284.

(46) Garcin, T., Rivoirard, S., Gaucherand, F. and Beaugnon, E., '*Kinetic Effects of Magnetic Field on the γ/α Interface Controlled Reaction in Iron',* Journal of Applied Physics, vol.107, 2010, 103903.

(47) Koyama, T. and Onodera, H., '*Phase-Field Modeling of Structural Elongation and Alignment of (α+γ) Microstructure in Fe-0.4C Alloy During Thermomagnetic Treatment'*, ISIJ International, vol.46, no.9, 2006, pp. 1277-1282.

(48) Ohtsuka, H., *'Structural Control of Fe-based Alloys Through Diffusional Solid/Solid Phase Transformations in a High Magnetic Field'*, Sci. Technol. Adv. Mater., vol.9, 013004, 2008, pp. 1-7.

(49) Fuji, H., '*Effects of Magnetic Field on Elemental Process for Microstructural Development of Iron-Based Polycrystalline Materials'*, PhD Thesis, 2009, Tohoku University, Japan.

(50) Nagamichi, S., Tsurekawa, S., Morizono, Y., Watanabe, T., Nishida, M. and Chiba., A., '*Diffusion of Carbon and Titanium in γ-iron in a Magnetic Field and a Magnetic Field Gradient'*, Journal of Materials Science, vol.40., 2005, pp. 3191-3198.

(51) Kadkhodabeigi, M., Saboohi, Y., '*New Model for MHD Instabilities in Aluminum Reduction Cells'*, Fifth International Conference on CFD in the Process Industries CSIRO, 2006.

(52) Bramfitt, B., L. and Benscoter, A., O., *'Metallographers Guide and Practices and Procedures for Irons and Steels',* ASM International, 2002, ISBN: 0-87170-748-9

(53) Karfoul, M., K., Tatlock, J., G. and Murray, R., T., '*The behavior of Iron and Aluminum During the Diffusion Welding of Carbon Steel to Aluminum',* Journal of Materials Science, vol.42, 2007, pp. 5692-5699

(54) '*Casting design and performance*', ASM International, ISBN-13: 978-0-87170-724-6, USA November 2009, p.225

(55) Da, S., Jincheng, L., Cast Irons Containing Rare Earths, Tsinghua University Academic Treatise, ISBN: 7-302-03918-6, 2000, p.220.

(56) Kurosawa, F., Taguchi, I., *Precipitation Behavior of Phosphides in the Centerline Segregation of Continuously Cast Steel Slabs*, Materials Transactions, JIM, vol.31, no.1, 1990, pp. 51-60.

(57) Predel, B.: *Fe-Na (Iron-Sodium)*. Madelung, O. (ed.). Springer Materials - The Landolt-Börnstein Database (http://www.springermaterials.com). DOI: 10.1007/10474837_1318

(58) Tricario, L., Spina, R., Sorgente, D. and Brandizzi, M., '*Effects of Heat Treatments on Mechanical Properties of Fe/Al explosion-welded Structural Transition Joints*', Materials and Design, vol.30, 2009, pp.2693-2700.

(59) Raghavan, V., '*C-Fe-P (Carbon-Iron-Phosphorous)*', Journal of Phase Equilibria and Diffusion, vol.25, no.6, 2004, pp. 541-542.

(60) Durand-Charre, M., *Microstructure of Steels and Cast Irons*, Springer, ISBN 3-540-20963-8, Paris, 2003.

(61) Metallography, Structures and Phase Diagrams, vol.8, Metals Handbook, 8th ed., American Society for Metals, 1973

(62) Pandit, A.S., '*Theory of Pearlite Transformations in Steels*', PhD Thesis, 2011, University of Cambridge.

(63) Failures Related to Casting, *Failure Analysis and Prevention*, ASM Handbook, ASM International, vol.11, 2002, pp.103-155.

APPENDIX

A1- Grid Numbers and corresponding median sizes (34)

Europe FEPA (93)	µm	
P50	336	Mean
P60	269	
P80	201	
P100	162	
P120	125	
P180	82	
P220	68	
P320	44.7-47.7	
P500:	28.7-31.7	
P800	20.8-22.8	
P1000	17.3-19.3	
P1200	14.3-16.3	
P2500	7.9-8.9	

A2: EDX analysis of the matrix surrounding the temper graphite in Figure 3.9

Element	Wt%
C	5.05
O	0.02
F	2.35
Na	0.00
Al	0.14
Si	1.58
P	0.31
S	0.00
Ca	0.02
Mn	0.45
Fe	90.08
Total:	**100.00**

A3: SEM images showing the side crack in the sample 6a

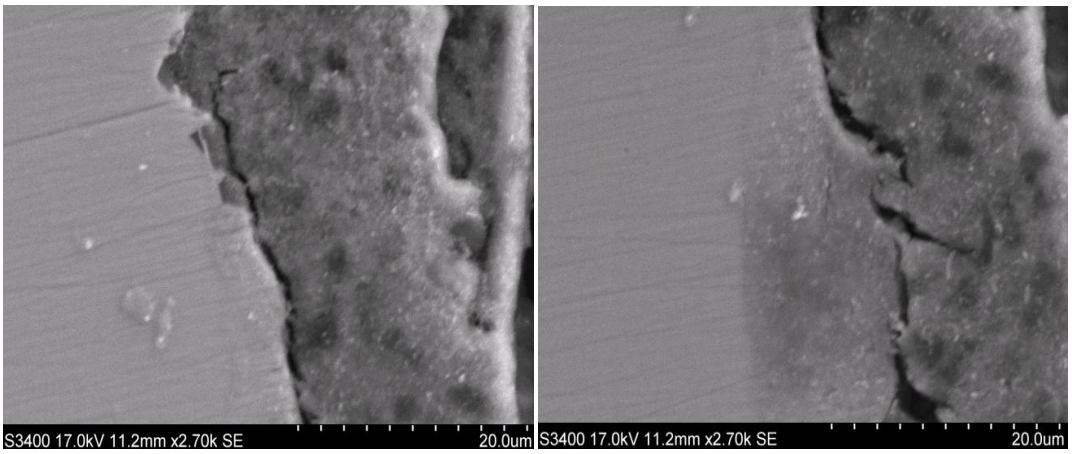

A4- Diffusion rate of carbon in α and γ iron (38)

Solute	**Frequency factor, D_0** (m^2s^1)		**Activation energy, Q** (kj/mol^{-1})		**Diffusion length** in 1 hour at 910^0C (μm)	
	in α	in γ	in α	in γ	in α	in γ
C	$1.27x10^{-6}$	$1x10^{-6}$	81.4	113	1080	192

A5- Volumetric change in high phosphorous cast irons as a function of temperature (32)

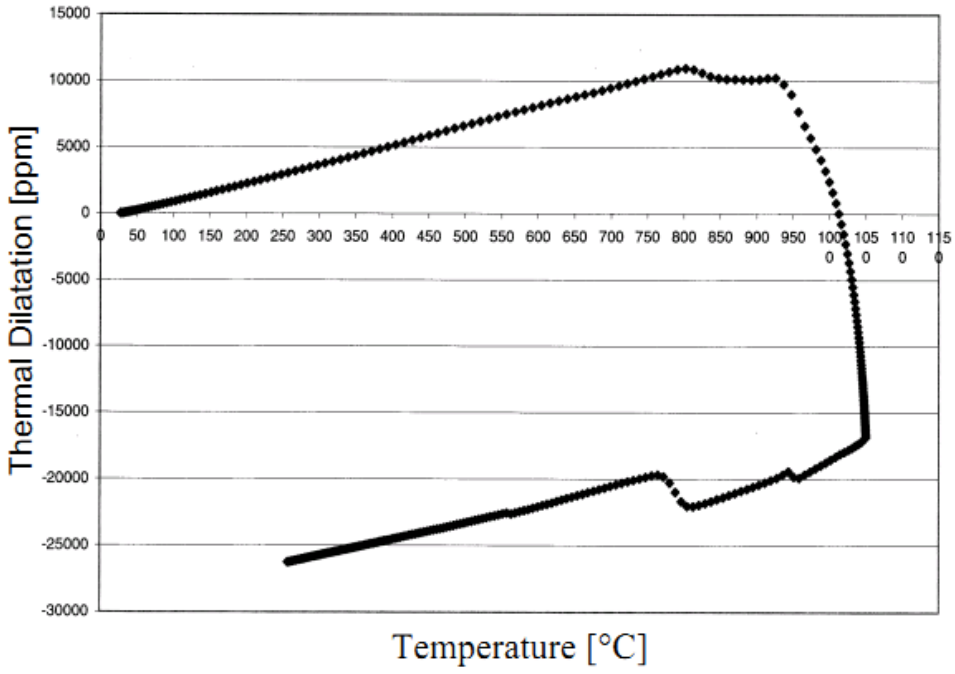

A6- Effect of the solute elements on the electrical conductivity of austenitic steels (42)

Element	Concentration range in the experiments	Element resistivity, ρ at 20^0C (nΩm/wt%)
C	0-0.1	521
Cr	14.7-26.9	21
N	0-0.2	1055
Si	0.1-2.2	254

A7- Electrical conductivity of cast irons containing different graphite morphologies (43)

Sample	Conductivity, σ $(10^6\ S\ m^{-1})$
Flake graphite	1.36 ± 0.05
Vermicular graphite	1.68 ± 0.08
Nodular graphite	1.88 ± 0.05

A8- EDX analysis of the steel within the sample 6a

Element	wt%
C	4.02
F	2.28
Na	0.02
Al	0.44
Si	0.10
P	0.03
S	0.11
Mn	0.39
Fe	92.61
Total:	**100.00**

A9- Equilibrium Fe-Na binary phase diagrams (57)

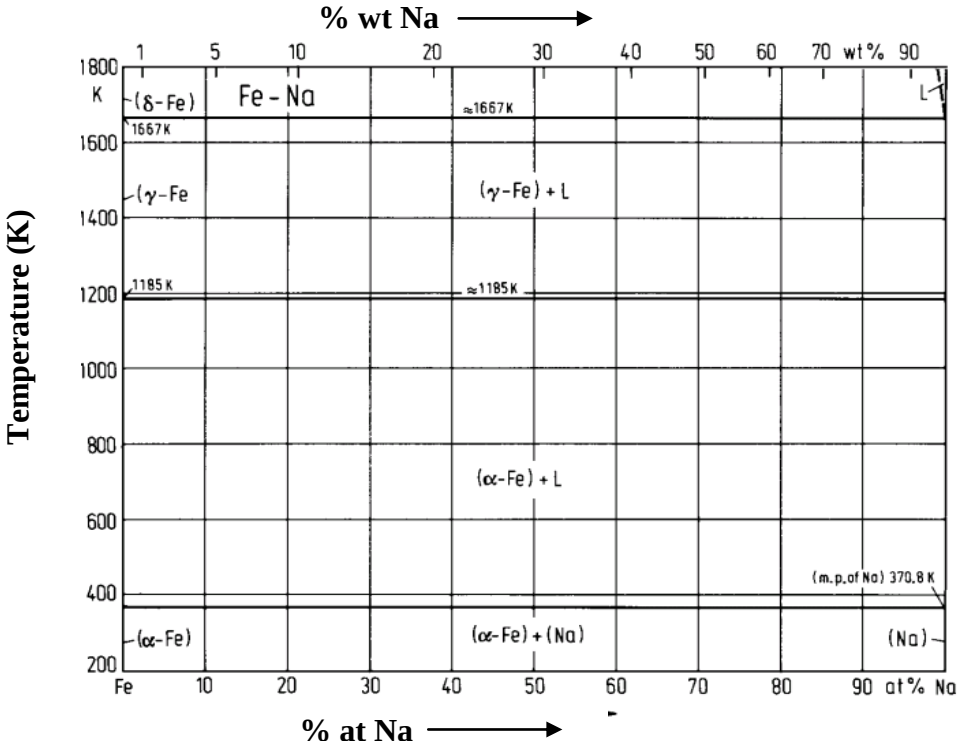

A10- Equilibrium Fe-Al binary phase diagram (58)

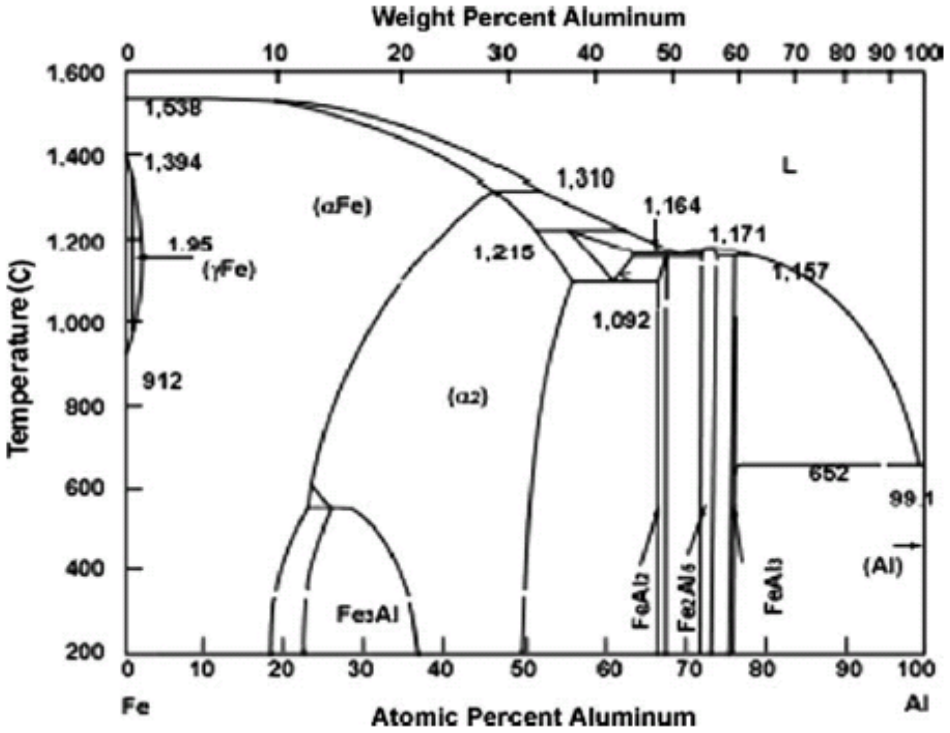

A11- Equilibrium phase diagrams for Fe-P and Fe-C-P systems. a) Fe-C b) isothermal section of Fe-P-C at 1000^{0}C, c) isothermal section of Fe-P-C at 900^{0}C, d) vertical section of Fe-P-C at P = 0.1wt% (59)

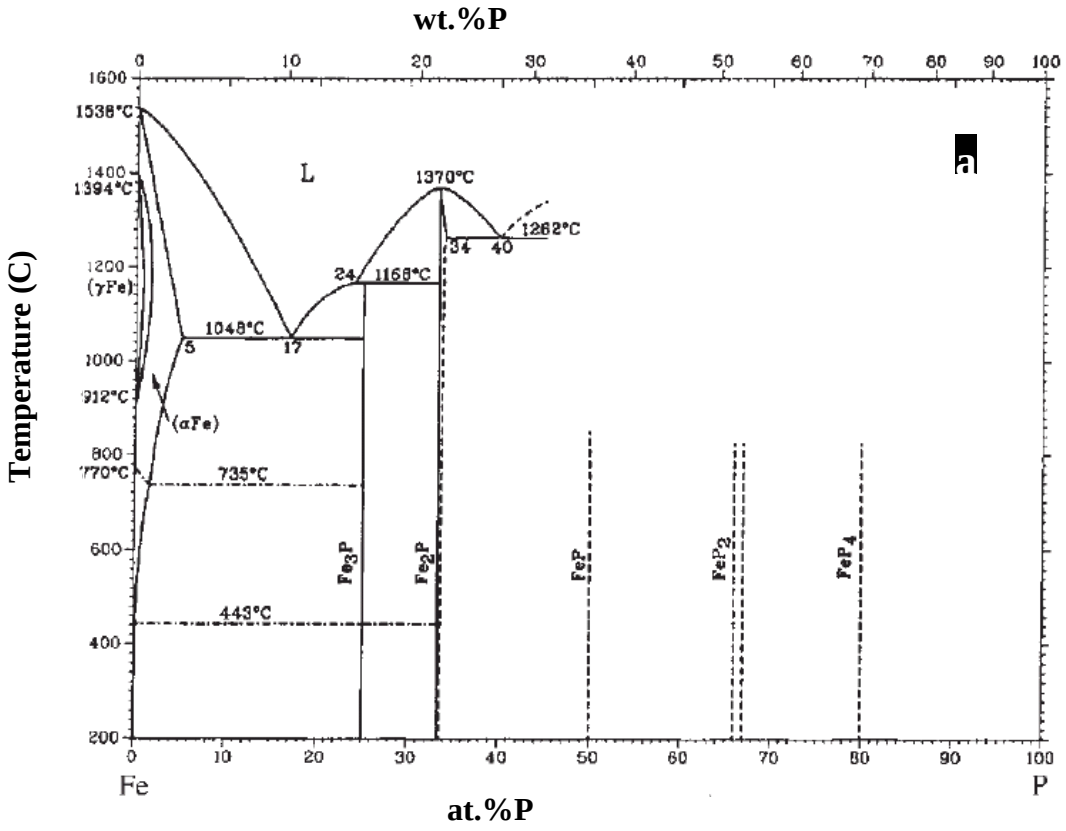

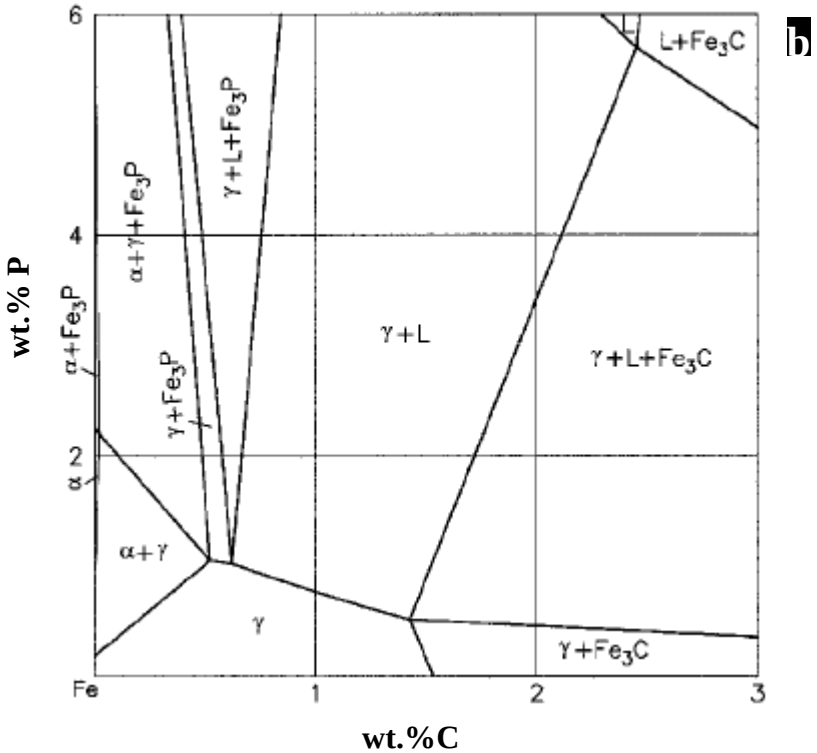

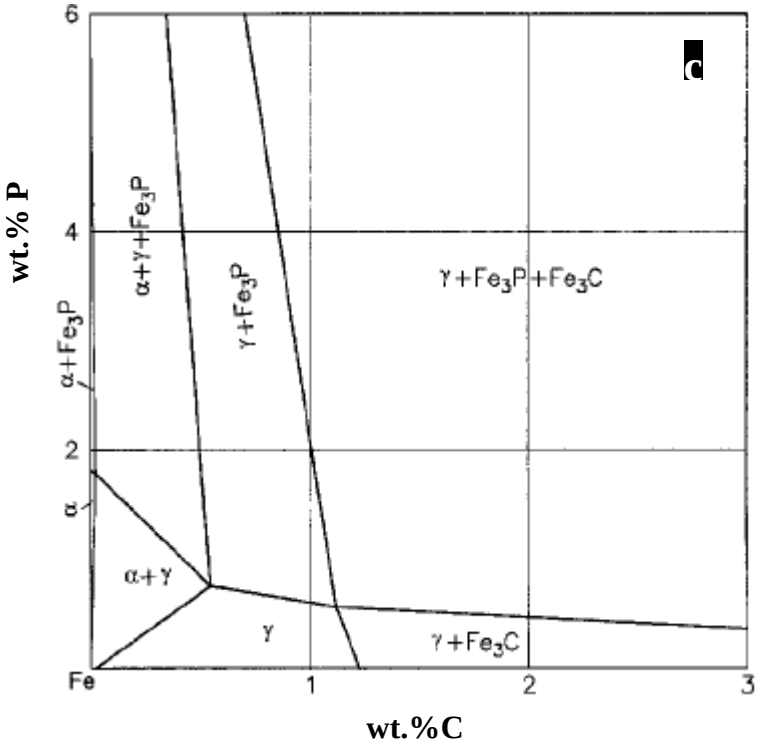
c
wt.% P
6
4
2
α
α+Fe3P
α+γ+Fe3P
γ+Fe3P
γ+Fe3P+Fe3C
α+γ
γ
γ+Fe3C
Fe
1
2
3
wt.%C

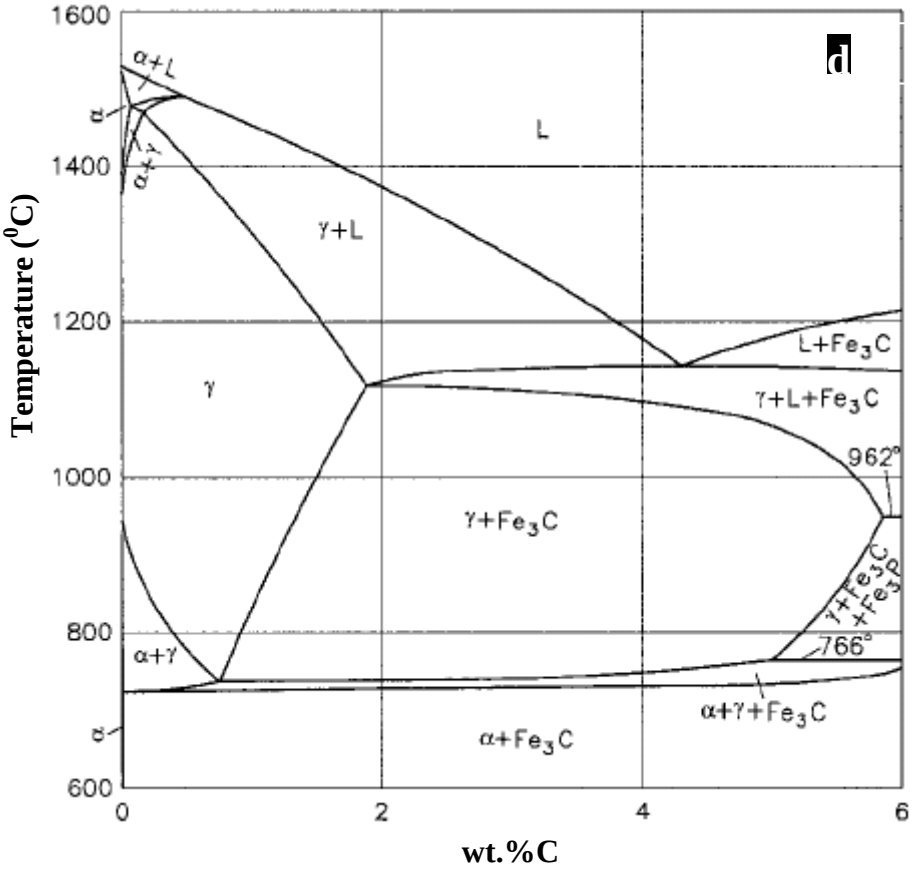
d
Temperature (0C)
1600
1400
1200
1000
800
600
α+L
α
α+γ
L
γ+L
γ
L+Fe3C
γ+L+Fe3C
962°
γ+Fe3C
γ+Fe3C+Fe3P
766°
α+γ
α+γ+Fe3C
α+Fe3C
0
2
4
6
wt.%C

B-Microstructure of Steels and Cast Irons

B.1- Basic Iron Steel Metallurgy

In the present section an attempt will be made to present the basis of microstructures encountered in cast irons and steels. For this purpose, it is beneficial to give an insight into the allotropic forms of pure iron;

- Body-centered cubic (BCC), α-Fe ≤ 912^0 C
- Face-centered cubic (FCC), γ-Fes 912-1394^0 C and,
- Body-centered cubic (BCC), δ-Fe 1394-1538^0 C

In steels, the alloys of C with these allotropes are termed *"Ferrite, Austenite and Delta Ferrite"* respectively. The equilibrium Fe-C phase diagram is given in Figure B-1. Note that the diagram is constructed up to the cementite composition, 6.67wt%C, because the composition of steels and cast irons used in most of the practical applications lie within 0-6.67wt%C range of the diagram. The first thing one should bear in mind is that Fe-C system exhibits a stable/metastable behavior and whether the specimen follows metastable or stable behavior depends on the alloying elements and the solidification rate (60). The products of metastable and stable paths are cementite and carbide respectively. Relatively rapid cooling promotes the cementite while slow cooling rates promotes graphite.

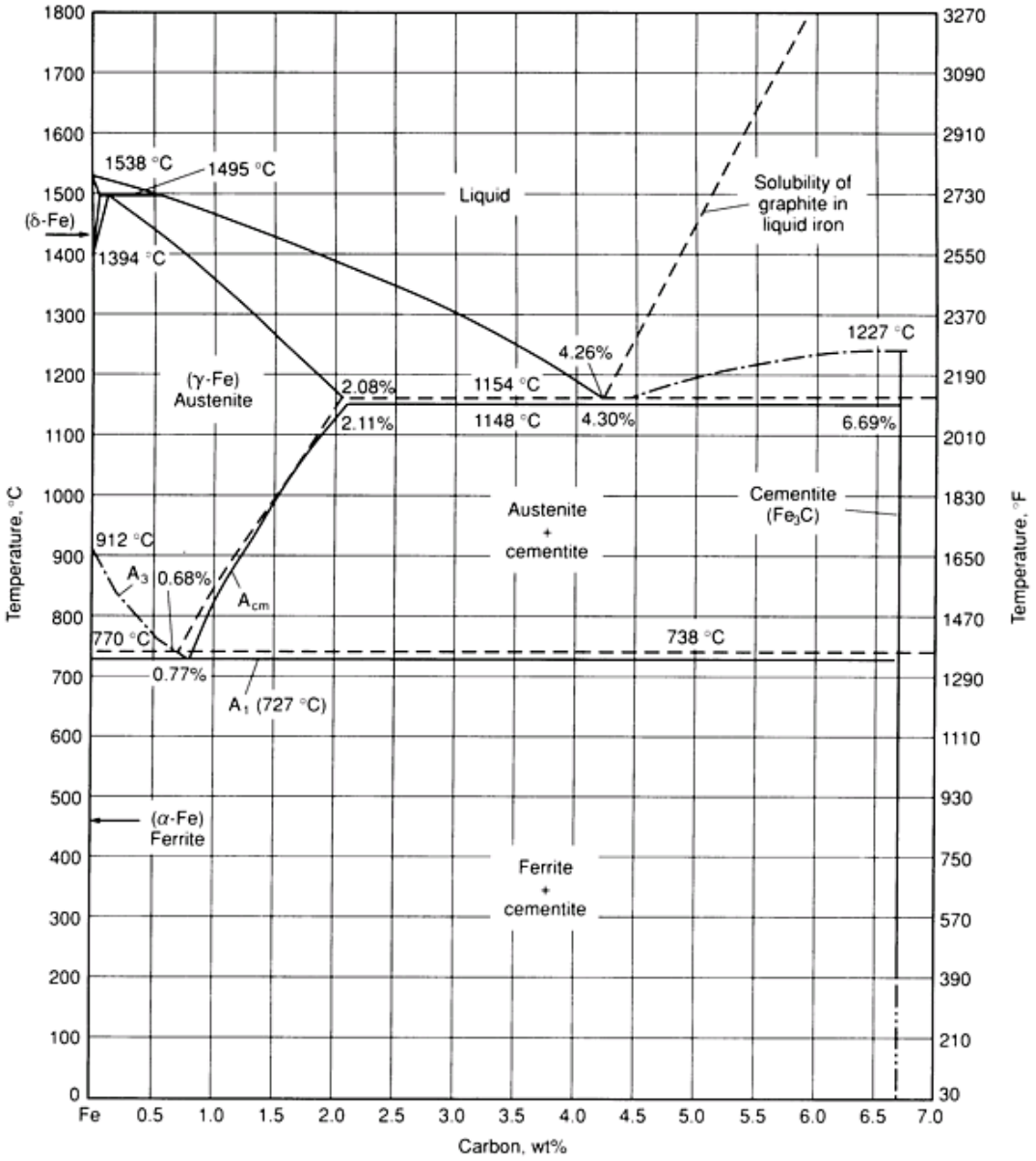

Figure B.1: Fe-C equilibrium diagram. Solid lines indicate Fe-Fe_3C metastable diagram, while dashed lines indicate stable Iron-Graphite diagram (61)

Steels, in simplest description, are the Fe-C alloys where the C content ranges between 0.008-2.14 wt%, usually less than 1 wt% and contain both ferrite and cementite at room temperature (no heat treatment). Owing to the presence of eutectoid point at 0.83 wt%C, steels are classified as hypoeutectoid, eutectoid and hypereutectoid steels.

When an Fe-C alloy of eutectoid composition is cooled down in conditions where equilibrium is maintained , a characteristic lamellar structure, pearlite, is formed as a result of eutectoid reaction (reaction b1) below the invariant equilibrium temperature. Pearlitic

structures when viewed in three dimensions, composes of interpenetrating ferrite and cementite crystals (62). Its appearance in planar sections is a lamellar structure.

$$\gamma \Rightarrow \alpha + Fe_3C \qquad \text{[b1]}$$

In the case of a liquid alloy of hypoeutectoid composition, the liquid alloy will transform into a solid with grains of lamellar structure with proeutectoid ferrite at the grain boundaries. Similarly the alloy of hypereutectoid composition will yield a microstructure similar to those found in hypoeutectoid structure, but with proeutectoid cementite, Fe_3C, at the grain boundaries.

The other important invariable reaction in the diagram is the eutectic reaction which is given by;

$$Liquid \Rightarrow \gamma + C_{graphite} \qquad \text{[b2]}$$

or,

$$Liquid \Rightarrow \gamma + Fe_3C \qquad \text{[b3]}$$

depending on whether the conditions endorse the system to follow the stable or metastable path respectively. It should be emphasized that both temperature and composition for eutectoid and eutectic reactions slightly differ from each other as illustrated in Figure B.1.

B.2- Microstructure of Cast Irons

We mentioned earlier that solidification and cooling rates are the decisive factors in resulting microstructures in cast irons. To better express and illustrate the importance of these factors and distinguish the resulting microstructures, we find it useful to have a question/answer section in which the given micrographs are interpreted with regards to their composition and cooling rate.

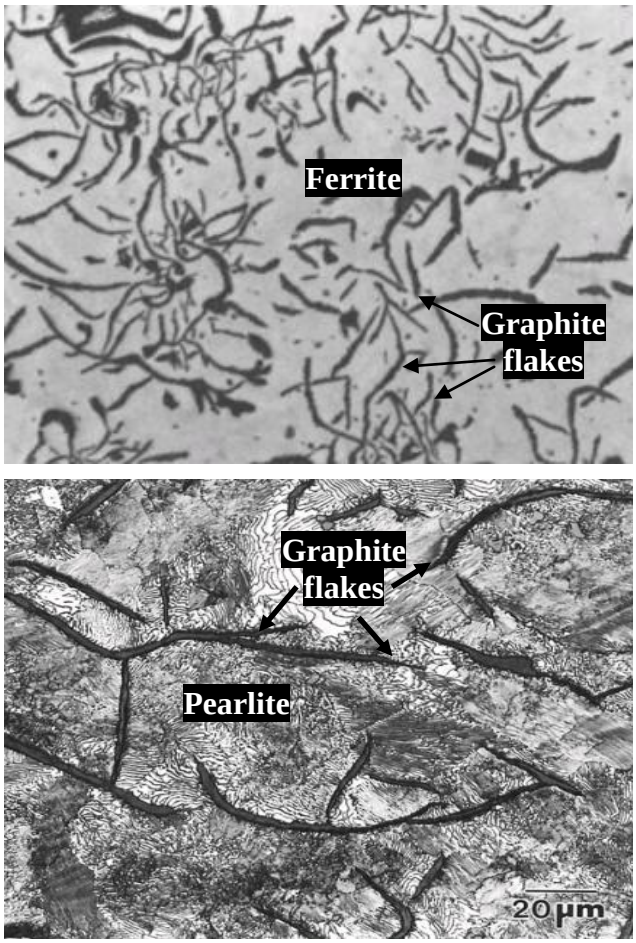

Figure B.2: Grey cast iron **a)** Ferritic matrix (63) **b)** Pearlitic matrix (52)

Figure B.2-a shows a typical ferritic grey cast iron. Graphite is precipitated as flakes embedded into a ferritic matrix. This microstructure is a result of equilibrium cooling where the liquid solidifies into austenite plus flake graphite. Upon further cooling to eutectic temperature, austenite decomposes into ferrite plus graphite. Figure B.2-b shows a pearlitic grey cast iron, where the graphite is precipitated as flakes in a ferritic matrix. Upon solidification liquid solidifies into austenite plus graphite as in Figure B2-a. However in this case solidification rate at eutectic temperature was rather fast so that cementite could not reach the graphite flakes but retained in pearlite. As we discussed earlier, pearlite is not a single phase, but a mixture of two phases (ferrite + cementite). When the cooling rate is high, cementite remains in the pearlite rather than reaching the graphite resulting in flake graphites in pearlitic matrix.

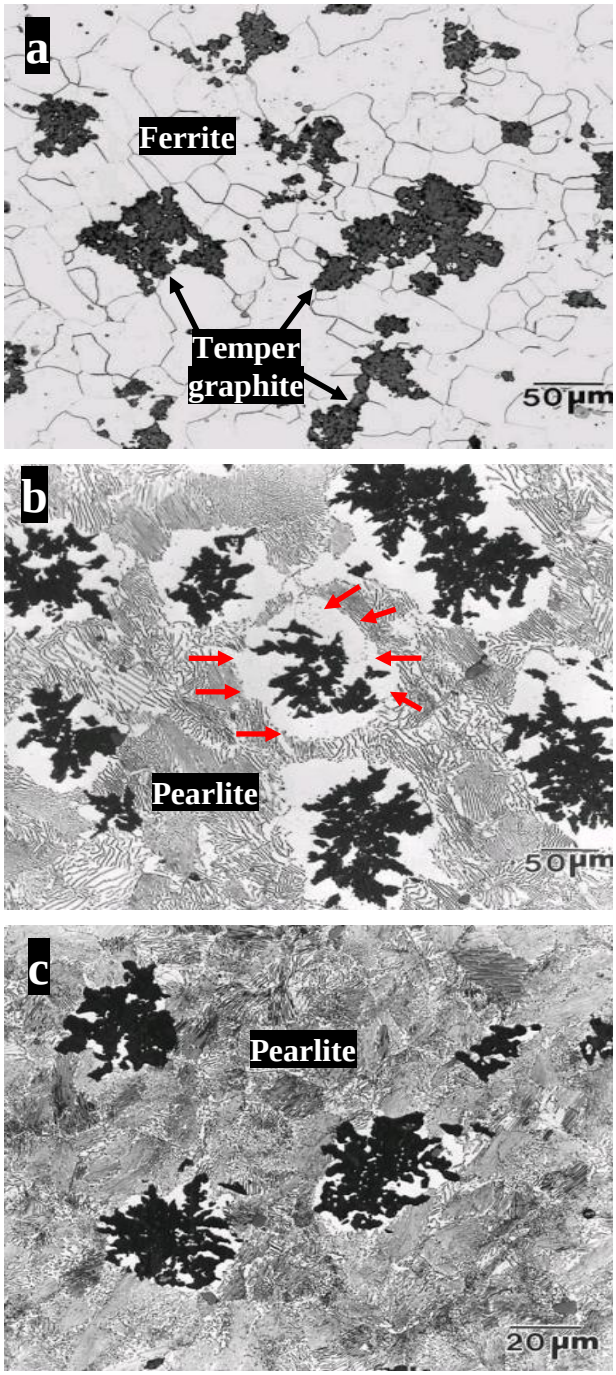

Figure B.3: Micrographs (52) of Malleable cast iron **a)** Ferritic matrix **b)** Pearlitic matrix with ferrite surrounding the temper graphite
c) Fully pearlitic matrix

Figure B.3-a shows a malleable cast iron structure in which the irregularly shaped graphite (temper graphite) is distributed in a ferritic matrix. This is a result of malleabilizing process where the cementite in white cast iron decomposes into temper graphite plus austenite at an annealing temperature of 900-970^{0}C (52). Upon cooling at a slow rate, at the eutectoid temperature, austenite decomposes into ferrite plus graphite and graphite precipitates onto the temper graphite (Figure B.3-a). The phases form at the eutectoid temperature may vary depending on the cooling rate. Because the carbon is repelled from the austenite upon cooling, in the case of mediate cooling rate, in the vicinity of temper graphite is formed ferrite (red arrows) while the matrix is composed of pearlite as shown in Figure B.3-b. This is simply because carbon around the temper graphite has a shorter diffusion length to the graphite while the carbon away from the temper graphite can not reach the temper graphite and formed pearlite with the ferrite. When the cooling rate is rapid, carbon can not reach the temper graphite and gives rise to a fully pearlitic matrix as shown in Figure B.3-c.